

Research Articles: Systems/Circuits

Generation and characterisation of a cell-type specific, inducible Cre-driver line to study olfactory processing

<https://doi.org/10.1523/JNEUROSCI.3076-20.2021>

Cite as: J. Neurosci 2021; 10.1523/JNEUROSCI.3076-20.2021

Received: 7 December 2020

Revised: 28 May 2021

Accepted: 1 June 2021

This Early Release article has been peer-reviewed and accepted, but has not been through the composition and copyediting processes. The final version may differ slightly in style or formatting and will contain links to any extended data.

Alerts: Sign up at www.jneurosci.org/alerts to receive customized email alerts when the fully formatted version of this article is published.

Copyright © 2021 Koldaeva et al.

This is an open-access article distributed under the terms of the Creative Commons Attribution 4.0 International license, which permits unrestricted use, distribution and reproduction in any medium provided that the original work is properly attributed.

1 Generation and characterisation of a cell-type specific, inducible Cre-driver line to study
2 olfactory processing

3
4 Abbreviated title: Mitral cell-specific inducible Cre-driver line

5
6 Anzhelika Koldaeva^{1†}, Cary Zhang^{1†}, Yu-Pei Huang^{1†}, Janine K Reinert¹, Seiya Mizuno², Fumihiko Sugiyama²,
7 Satoru Takahashi², Taha Soliman¹, Hiroaki Matsunami³, Izumi Fukunaga^{1*}

8
9 ¹Sensory and Behavioural Neuroscience Unit, Okinawa Institute of Science and Technology Graduate
10 University

11 ²Laboratory Animal Resource Center, Tsukuba University

12 ³Department of Molecular Genetics and Microbiology and Department of Neurobiology, Duke University

13
14 [†]These authors contributed equally.

15 * To whom correspondence should be addressed (Izumi.fukunaga@oist.jp).

16 17 18 **Abstract**

19
20 In sensory systems of the brain, mechanisms exist to extract distinct features from stimuli to generate a variety
21 of behavioural repertoires. These often correspond to different cell types at various stages in sensory
22 processing. In the mammalian olfactory system, complex information processing starts in the olfactory bulb,
23 whose output is conveyed by mitral and tufted cells (MCs and TCs). Despite many differences between them,
24 and despite the crucial position they occupy in the information hierarchy, Cre-driver lines that distinguish
25 them do not yet exist. Here, we sought to identify genes that are differentially expressed between MCs and
26 TCs of the mouse, with an ultimate goal to generate a cell-type specific Cre-driver line, starting from a
27 transcriptome analysis using a large and publicly available single-cell RNA-seq dataset (Zeisel et al., 2018).
28 Many genes were differentially expressed, but only a few showed consistent expressions in MCs and at the
29 specificity required. After further validating these putative markers using *in-situ* hybridization, two genes,
30 namely *Pkib* and *Lbdh2*, remained as promising candidates. Using CRISPR/Cas9-mediated gene editing, we
31 generated Cre-driver lines and analysed the resulting recombination patterns. This indicated that our new
32 inducible Cre-driver line, *Lbdh2-CreERT2*, can be used to genetically label MCs in a tamoxifen dose-dependent
33 manner, both in male and female mice, as assessed by soma locations, projection patterns and sensory-evoked
34 responses *in vivo*. Hence this is a promising tool for investigating cell-type specific contributions to olfactory
35 processing and demonstrates the power of publicly accessible data in accelerating science.

36 37 **Significance statement**

38
39 In the brain, distinct cell types play unique roles. It is therefore important to have tools for studying unique
40 cell types specifically. For the sense of smell in mammals, information is processed first by circuits of the
41 olfactory bulb, where two types of cells, mitral cells and tufted cells, output different information. We
42 generated a transgenic mouse line that enables mitral cells to be specifically labelled or manipulated. This was
43 achieved by looking for genes that are specific to mitral cells using a large and public gene expression dataset,

44 and creating a transgenic mouse using the gene editing technique, CRISPR/Cas9. This will allow scientists to
45 better investigate parallel information processing underlying the sense of smell.

46

47 **Introduction**

48

49 The complexity of the brain, in part, originates from the diversity of its components, the rich variety of cells.
50 This diversity is evident in morphology, connectivity, molecular expression profiles, and biophysical properties
51 (Sanes and Masland, 2015; Zeng and Sanes, 2017; Luo et al., 2018), which together give rise to what we refer
52 to as cell types. Because the differences are thought to reflect distinct computational tasks or functions
53 (Masland, 2004; Luo et al., 2018), the ability to selectively identify, and to manipulate, each cell type
54 experimentally is key to understanding how the brain works.

55

56 In rodents, complex, synaptic processing of olfactory information in the brain first occurs in the olfactory bulb.
57 The principal cells of the olfactory bulb, the MCs and TCs, convey the output of this region and are thought to
58 form parallel information streams. They differ in a variety of anatomical and physiological properties
59 (Fukunaga et al., 2012; Igarashi et al., 2012; Phillips et al., 2012; Otazu et al., 2015; Economo et al., 2016;
60 Kapoor et al., 2016; Jordan et al., 2018). MCs, which are the larger of the two, are thought to form distinct
61 circuits with local neurons from those formed by TCs (Mori et al., 1983; Fukunaga et al., 2012; Phillips et al.,
62 2012; Geramita et al., 2016), some of which may explain the differences in how they encode odors. For
63 example, in TCs, the timing of responses adheres strictly to a specific phase of the sniff cycle, while MCs
64 modulate the timing widely over the entire sniff cycle (Fukunaga et al., 2012; Igarashi et al., 2012; Ackels et
65 al., 2020). Signal integration over this long temporal window is thought to allow MCs to represent more
66 complex information (Fukunaga et al., 2012). Further, in contrast to TCs whose axons project to a more limited
67 portion of the olfactory cortex, the target areas of MCs range widely, extending as far as the posterior piriform
68 cortex, the cortical amygdala, and the lateral entorhinal cortex (Haberly and Price, 1977; Igarashi et al., 2012),
69 indicative of a variety of behavioural contexts in which MCs are likely to be important.

70

71 Despite the fundamental roles these two cell types play in olfaction, suitable molecular markers and genetic
72 tools are lacking. Molecules commonly used to label the output neurons of the olfactory bulb include
73 protocadherin-21 (Nagai et al., 2005), T-box transcription factor 21 (*Tbx21*, also known as *Tbet*; (Papaioannou
74 and Silver, 1998; Faedo et al., 2002)), as well as cholecystokinin (*Cck*) (Seroogy et al., 1985). In the brain, *Tbx21*
75 is expressed from embryonic day 14 (Faedo et al., 2002) and is exclusive to the principal neurons of the
76 olfactory bulb, labeling both MCs and TCs (Faedo et al., 2002; Mitsui et al., 2011; Haddad et al., 2013). In
77 contrast, *Cck* is expressed widely in the brain (Larsson and Rehfeld, 1979; Taniguchi et al., 2011). In the
78 olfactory bulb, expression occurs preferentially in TCs over MCs (Seroogy et al., 1985), which has been utilized
79 for analysing the unique physiology of TCs (Economo et al., 2016; Short and Wachowiak, 2019). These
80 overlapping but differential expression patterns between *Cck* and *Tbx21* may be useful in discovering more
81 selective markers to distinguish the two types of principal neurons.

82

83 A variety of methods now exist to analyse gene expression patterns in relation to cell types, including *in-situ*
84 hybridization (Lein et al., 2006), as well as transcriptomic approaches that retain spatial information, with
85 increasing resolution (Ståhl et al., 2016). More recently, single-cell RNA sequencing (scRNA-seq) (Sugino et al.,

86 2006; Tang et al., 2009; Pfeffer et al., 2013; Zeisel et al., 2015; Shekhar et al., 2016; Tasic et al., 2016) has seen
87 rapid developments, which have enabled the investigation of cell-type specific gene expression patterns with
88 unprecedented levels of detail and scale (Lein et al., 2017; Zeng and Sanes, 2017). A useful application of this
89 information in turn may be to generate transgenic driver lines, that allow a particular cell type to be extensively
90 studied. The availability of Cre-driver lines has been instrumental in revealing unique functions of distinct cell
91 types, across multiple levels of analyses (Gong et al., 2003; Taniguchi et al., 2011; Madisen et al., 2012; Dhande
92 et al., 2013; Cruz-Martín et al., 2014; Wolff et al., 2014; Madisen et al., 2015; Sanes and Masland, 2015; Daigle
93 et al., 2018).

94

95 Here, we take advantage of a large dataset that has become publicly available (Zeisel et al., 2018), to discover
96 markers that distinguish between MCs from TCs. The results of the analyses allowed us to generate, and
97 characterize, new Cre-driver lines. Such molecular tools will be key to understanding the mechanisms of
98 olfactory perception and behaviour.

99

100 **Methods**

101

102 *Gene expression data*

103 Single-cell RNA sequencing data from the mouse brain was obtained from Zeisel et al (Zeisel et al., 2018)
 104 in Loom format. We used the dataset from the level 2 analysis that correspond to the olfactory neurons.
 105 The gene expression table represents the expression levels of 27,998 genes in 10,745 olfactory bulb cells.
 106 The gene expression level, which counts the number of expressed genes, was transformed into
 107 $\log_2(\text{count}+1)$ before analysing further.

108

109 *Dimensionality reduction:* We screened for genes that have higher variability than expected by calculating
 110 a log-transformed Fano factor for each gene, as previously described (Li et al., 2017):

111

$$112 \quad F(x) = \log_{10} \left[\frac{\sigma^2(x)}{\mu(x)} \right],$$

113

114

115 where $\mu(x)$ and $\sigma^2(x)$ are the mean and the variance of the expression level across cells respectively.
 116 Then using the mean expression across different cells, we split the genes into 20 subsets and calculate the
 117 Z-score of the Fano factor within each subset:

118

$$119 \quad Z(x) = \frac{[F(x) - \text{mean}(F(x))]}{\text{std}[F(x)]},$$

120

121 where $\text{mean}(F(x))$ and $\text{std}[F(x)]$ are the mean and the standard deviation of $F(x)$ within the subset. The
 122 top 500 genes with the highest value of $Z(x)$ were used to cluster the gene expression data. To visualise
 123 and cluster the gene expression data corresponding to individual cells in 2D space, we reduce the
 124 dimensionality using the principal component analysis (PCA) and t-distributed Stochastic Neighbor
 125 Embedding (tSNE; (van der Maaten and Hinton, 2008)). We used top 10 principal components to run tSNE
 126 with the following parameters: learning rate = 10, perplexity = 33. The result is shown in Fig. 1. Since many
 127 genes have similar expression patterns across different cells, in order to increase the power of PCA and
 128 tSNE, we extracted overdispersed genes i.e., the most informative genes.

129

130 *Clustering:* Using the 2-dimensional data above, hierarchical clustering algorithm HDBSCAN (Campello et
 131 al., 2013) was performed with the following parameters: `min_clust_size = 5`, `min_pts = 13`, which indicates
 132 which nearest neighbor to use for calculating the core-distances of each point. The cluster with the highest
 133 expression level of *Tbx21* gene contained 101 cells. Within this group, clustering with HDBSCAN on tSNE
 134 space revealed 4 clusters. We then compared the *Cck* expression level across the clusters. We found that
 135 18% (2 of 11) of cells from cluster #4 express *Cck* above the threshold = 3 ($\log_2(\text{count}+1)$), while 64% (58
 136 of 90) from clusters #1, #2 and #3 express *Cck* above the threshold, thus we defined the cluster #4 to be
 137 the putative MC cluster.

138

139 *Differential expression analysis and identification of molecular markers:* We used the Mann-Whitney U-
140 test to find differently expressed genes. The test works under the assumption that the samples are
141 independent. P-values were adjusted using the Benjamini-Hochberg procedure. We screened for
142 significant genes, with the adjusted p value below the threshold = 0.05, where its median expression level
143 in the MC cluster above the threshold = 3 in more than 50% of the cells. Of these, genes that are highly
144 expressed in non-MC clusters were eliminated (cut-off of 10% of cells).

145

146 **Animals**

147 All animal experiments were approved by the animal experiment ethics committee of OIST Graduate
148 University (protocol: 2018-201) and University of Tsukuba. ICR and C56BL/6J mice were purchased from
149 Laboratories International, Inc. (Yokohama, Japan) for generation of transgenic mice, and C56BL/6J from
150 Japan CLEA (Shizuoka, Japan) for subsequent breeding. Ai14 (Madisen et al., 2010) were from The Jackson
151 Laboratory (Bar Harbor, USA), and Ra13-Cre was from the GENSAT project (Gong et al., 2003), via MMRRC
152 (MBP, University of California, Davis). Mice of either sex were used in this study.

153

154 *Generation of Pkib-IRES-cre and Lbhd2-IRES-CreERT2 mice*

155 Vector construction for knock-in mouse production: The CRISPR target sequence (5'-
156 ATAGCAGCTATGTATTCCTGGGG-3') was selected for integration of the IRES-Cre sequence just after the
157 stop codon of *Pkib* and *Lbhd2*. The *pX330* plasmid, carrying both gRNA and Cas9 expression units, was a
158 gift from Dr. Feng Zhang (Addgene plasmid 42230) (Cong et al., 2013). The oligo DNAs (Pkib-CRISPR F: 5'-
159 caccATAGCAGCTATGTATTCCTG-3', and Pkib-CRISPR R : 5'-aacCAGGAATACATAGCTGCTAT-3') were
160 annealed and inserted into the entry site of *pX330* as described previously (Mizuno et al., 2014). This
161 plasmid was designated as *pX330- Pkib*. The donor plasmid *pIRES-Cre-Pkib* contained the IRES sequence
162 (Bochkov and Palmenberg, 2006), nuclear translocation signal (NLS)-Cre, and rabbit globin
163 polyadenylation signal sequence. The 1.6-kb 5'-arm (from 1521 bp upstream to 64 bp downstream of *Pkib*
164 stop codon) and the 2.0-kb 3'-arm (from 65 bp downstream to 2,038 bp downstream of *Pkib* stop codon)
165 were cloned into this vector. DNA vectors (*pX330- Pkib* and *pIRES-Cre-Pkib*) were isolated with a FastGene
166 Plasmid mini Kit (Nippon Genetics, Tokyo, Japan) and filtrated by MILLEX-GV 0.22 μ m Filter unit (Merk
167 Millipore, Darmstadt, Germany) for microinjection. Mice were kept in IVC cages under specific pathogen-
168 free conditions in a room maintained at 23.5°C \pm 2.5°C and 52.5% \pm 12.5% relative humidity under a 14-h
169 light:10-h dark cycle. Mice had free access to commercial chow (MF diet; Oriental Yeast Co., Ltd., Tokyo,
170 Japan) and filtered water.

171

172 *Microinjection and Genomic DNA analyses*

173 The pregnant mare serum gonadotropin (5 units) and the human chorionic gonadotropin (5 units) were
174 intraperitoneally injected into female C57BL/6J mice with a 48-h interval and mated with male C57BL/6J
175 mice. We collected zygotes from oviducts in mated females and a mixture of the *pX330- Pkib* (circular, 5
176 ng/ μ L) and *pIRES-Cre-Pkib* (circular, 10 ng/ μ L) plasmids was microinjected into 148 zygotes. Subsequently,
177 surviving 137 injected zygotes were transferred into oviducts in pseudopregnant ICR females and 21 pups
178 were obtained.

179

180 To confirm the knock-in mutation, the genomic DNA were purified from the tail samples using the PI-200
181 DNA extraction kit (Kurabo Industries LTD, Osaka, Japan) according to manufacturer's protocol. Genomic
182 PCR was performed with KOD-Fx (TOYOBO, Osaka, Japan). The primers (Cre forward: 5'-
183 TCTGAGCATACCTGGAAAATGCTTCTGT-3', and Pkib reverse: 5'-GTACCAGGAGCTCAAGACAACCTTACCC-3')
184 were used for checking the 5' side correct knock-in and the primers (Pkib forward: 5'-
185 CTATTCACAGGTCCAGTTGCTGAAACC-3', and Cre reverse: 5'-ACAGAAGCATTTTCCAGGTATGCTCAGA-3')
186 were used for checking the 3' side correct knock-in. We found 5 of 21 founders carried the designed knock-
187 in mutation. In addition, we checked random integration of *pX330-Pkib* and *pIRES-Cre-Pkib* by PCR with
188 ampicillin resistance gene detecting primer (Amp detection-F: 5'-TTGCCGGGAAGCTAGAGTAA-3', and Amp
189 detection-R: 5'-TTGCCTTCTGTTTTGCT-3') and no founder carried the random integration allele.

190

191 **Histology**

192 *In situ hybridisation:* ISH was performed using the RNAscope ISH system (ACDBio, Newark, CA, USA)(Wang
193 et al., 2012).

194

195 *Brain extraction:* Whole brains were extracted and immediately placed in 4% PFA, dissolved in phosphate
196 buffer (225.7 mM NaH₂PO₄, 774.0 mM Na₂HPO₄, pH 7.4) at 4°C for 24 hours. Subsequently, the tissues
197 were sunk in DEPC-treated 30% sucrose solution (~2 days), then embedded in OCT (4583, Sakura Finetech,
198 Japan) in a cryomold (Peel-A-Way, Sigma-Aldrich) to be frozen in an ethanol/dry ice bath and stored at -
199 80°C until use.

200

201 *Probe design:* ISH was carried out using RNAscope (ACDBio, Newark, CA, USA) and probes were produced
202 by ACDBio to be compatible for the procedure. Sequence regions for the *Pkib* and *Ldhd2* probes were
203 selected using the NCBI genetic database. For both probes, regions that were common to all splice variants
204 of each gene were selected. The *Pkib* probe targeted the region 141-973 bp of the transcript
205 XM_006512605.3. The *Ldhd2* probe targeted the region 138-715 bp of the transcript XM_006516048.1.
206 The *Tbx21* probe, which targets the region 893-2093 bp of the transcript NM_019507.2, was already
207 commercially available (403331, ACDBio, USA).

208

209 *Hybridisation:* On the day of ISH, coronal olfactory bulb sections (20 μm) were cut on a cryostat (Leica
210 CM3050S, Leica Biosystems) at -20°C, washed in RNase-free PBS (Corning, Manassas, VA, USA), and
211 immediately mounted on glass slides (Superfrost plus, Thermo Fisher Scientific, Waltham, USA). Slides
212 were dried for 30 min at 60°C and post-fixed for 15 min in 4% PFA at 4°C. Slides then underwent *in situ*
213 hybridisation using RNAscope reagents, according to manufacturer's protocols. Unless otherwise stated,
214 all reagents were provided in the RNAscope kit (RNAscope Intro Pack 2.5 HD Reagent Kit Brown-Mm, Cat
215 no. 322371). Briefly, slides were dehydrated through an ethanol series (75%, 90%, 100%, 100%, Sigma-
216 Aldrich) and endogenous peroxidase activity blocked using provided hydrogen peroxide for 10 min at
217 room temperature. Sections then underwent antigen retrieval by submersion into boiling (~98-102°C) 1X
218 Target Retrieval Solution for 5 min and were rinsed in distilled water by submerging 5 times. Subsequently,
219 slides were submerged into 100% ethanol 5 times and air dried. A barrier using an ImmEdge hydrophobic
220 barrier pen was drawn around the sections and left overnight at room temperature to dry. On the
221 following day, slides were treated with Protease Plus and incubated in an oven (HybEZ II System, ACDBio)

222 for 30 min, followed by a series of incubations in the same oven with provided solutions (AMP1-6) to
223 amplify probes (AMP1&3: 30 min at 40°C; AMP2&4: 15 min at 40°C; AMP5: 30 min at room temperature;
224 AMP6: 15 min at room temperature). After amplification, a DAB reaction was carried out (1:1 mixture of
225 DAB-A and DAB-B solutions, Vector Labs, California, USA) for 10 min at room temperature. Slides were
226 washed by submersion 5 times in 2 changes of distilled water.

227

228 *Counterstaining:* Olfactory bulb sections were immersed in Mayer's haematoxylin solution (MHS16,
229 Sigma-Aldrich) for 10 mins. Excess stain was washed in distilled water and sections were differentiated by
230 quick submersion in 0.2% ammonium hydroxide in distilled water, followed by washing for 5 minutes in
231 distilled water. Slides were then dehydrated through a series of ethanol for 5 mins each, followed by two
232 5 min immersions in xylene. Slides were then covered with DPX mountant (06522, Sigma-Aldrich) for
233 histology and left at room temperature to dry before imaging.

234

235 **Virus injection**

236 Three week-old, heterozygous *Lbhd2-IRES-CreERT2* mice were anaesthetised with isoflurane (IsoFlo,
237 Zoetis Japan, Shibuya, Tokyo, Japan) and placed on a stereotaxic frame (Kopf, Tujunga, CA, USA).
238 Carprofen (Rimadyl, Zoetis; s.c., 5mg/kg in saline) was injected subcutaneously for analgesia. The fur was
239 trimmed, and the skin was disinfected with 10% iodine solution before incision. A craniotomy was made
240 bilaterally over centre of the dorsal olfactory bulb (co-ordinates relative to Bregma: AP: 4.8 mm; ML: \pm 0.8
241 mm). 100 nL of AAV1-pCAG-Flex-EGFP-WPRE (Addgene, Watertown, MA, USA) was injected from a pulled
242 glass capillary tube (tip diameter approximately 10 μ m) at a depth 0.3 mm relative to the brain surface,
243 at a rate of 2 nL every 5 s, using a Nanoject III injector (Drummond Scientific, Broomall, PA, USA). Following
244 injection, the glass capillary was left in place for 1 minute and then slowly withdrawn. The surgical site
245 was then sutured, and mice allowed to recover in a warmed chamber until fully awake, before being
246 returned to their home cage. It is advisable that AAVs for conditional expression are tested before use, as
247 they can exhibit off-target, "leak" expressions depending on the production protocol (Fischer et al., 2019),
248 especially if not diluted enough.

249

250 **Tamoxifen administration**

251 Tamoxifen solution was dissolved at a concentration of 8 mg/mL in a solvent consisting of 5% ethanol and
252 95% corn oil (23-0320, Sigma-Aldrich), for once daily injections of 80 mg/kg (10 mL/kg injection volume).
253 Tamoxifen powder (T5648, Sigma-Aldrich) was initially suspended in 100% ethanol and mixed using a
254 vortex mixer to allow partial dissolution. Corn oil was subsequently added to make up solution to the final
255 volume and the solution was heated up to 60°C with agitation on an orbital mixer in an oven, with periodic
256 mixing on the vortex mixer. When fully dissolved (~30 min), the solution was cooled to room temperature,
257 and mice were injected intraperitoneally using a 23G needle with care taken to avoid bubble formations.
258 Injected mice were housed separately from untreated littermates. The mouse weights were monitored
259 carefully throughout the injection period as well as 3 days after the final injection to ensure recovery. For
260 a proof-of-principle P7 injections, 1 injection of 80 mg/kg was given using a 30G needle. A single-dose
261 protocol was used to minimise disturbance to the pups and the nursing mother. Gloves were rubbed with
262 the cage bedding prior to handling, and injected pups were returned to the cage with the mother.

263

264 Two-photon functional imaging

265 Cal-520 dextran (M.W. ~11,000, AAT Bioquest, Sunnyvale USA) was dissolved to 50 mg/mL in Ringer solution
266 comprising (in mM): NaCl (135), KCl (5.4), HEPES (5), MgCl₂ (1), CaCl₂ (1.8). Cal-520 dextran solution was
267 electroporated in the glomerular layer of the left OB of P42 *Lbhd2-CreERT2::Ai14* mice (tamoxifen dose = 3 x
268 80 mg/kg starting at P21), at a depth ~100 μm below the brain surface, under isoflurane anaesthesia.
269 Parameters of electroporation were set according to the low intensity protocol described in (Hovis et al., 2010).
270 Immediately after the electroporation, the craniotomy was sealed with an imaging window, and mice were
271 anaesthetized with ketamine/xylazine (100 mg.kg⁻¹/20 mg.kg⁻¹, i.p.) and two-photon imaging of dye-loaded TCs
272 and MCs were obtained with a custom two-photon microscope (INSS, South Chailey, UK) using 980 nm high-
273 power laser (Insight DeepSee, SpectraPhysics) fitted with a water-immersion 25x objective (CFI75 Apo 25XC W
274 1300, Nikon, Japan) and resonance scanner (30 Hz frame rate; field of view was 256 x 256 μm, 512 x 512 pixels).
275 MCs were those located ~ 300 μm below the brain surface (labeled = red fluorescent cells + green fluorescence,
276 unlabelled = loaded cells without red fluorescence), while TCs were smaller cells located more superficially.
277 Strongly fluorescent cells were excluded from analysis. 5 odours were presented in a randomized order using
278 a custom-made, flow-dilution olfactometer (Koldaeva et al., 2019), at approximately 5% of the saturated
279 vapour, while the total flow rate was 2 L/min. Odours used were ethyl butyrate, methyl tiglate, methyl butyrate,
280 acetophenone and methyl salicylate. Inter-trial interval was 30 seconds during which lines were purged with
281 pressurized air to minimise cross contamination. Due to bleaching and other time-dependent factors such as
282 the depth of anaesthesia, typically, 3-4 presentations were given for each odour. For GCaMP6f imaging, *Lbhd2-*
283 *CreERT2::Ai95D* mice were injected with tamoxifen intraperitoneally at P21 (1 x 160 mg/kg). After 2 weeks, the
284 mice were surgically implanted with a cranial window over the left olfactory bulb, as well as a head plate, and
285 allowed to recover. After 2 further weeks, they were anaesthetized with ketamine/xylazine, and head-fixed for
286 imaging. Odours were presented in the manner described above for the electroporation experiment, but 6
287 odours were presented with the order randomly permuted. The additional odour was butyl acetate. The body
288 temperatures of the mice were maintained at 36°C using a thermostat.

290 Confocal Imaging

291 Confocal images were acquired on a Zeiss LSM780 confocal microscope with a 10X objective (Zeiss, NA
292 0.45 Plan-Apochromat) for the whole brain sagittal sections, and 20X objective (Zeiss, NA 0.8 Plan-
293 Apochromat) for the olfactory bulb. Using ZEN 2.3 software (Zeiss), images were taken at a resolution of
294 1024 x 1024 pixels for a field of view of 850.19 μm x 850.19 μm (10X) or 425.1 μm x 425.1 μm (20X
295 objective). To enable comparison and quantification of viral injections, imaging conditions (resolution,
296 gain, laser power, number of averages) were kept consistent. Sequential laser excitation was used to
297 prevent fluorophore bleed-through. Images were taken throughout the whole rostro-caudal extent of
298 viral spread using the 20x objective. For axonal projection analysis, images were acquired using a Leica
299 SP8 confocal microscope using a 10X (Leica, NA 0.40 Plan-Apochromat) and a 40X (Leica, NA 1.3 Plan-
300 Apochromat) objective. Images were taken at a resolution of 1024 x 1024 pixels per field of view (10X:
301 1163.64 x 1163.64 μm; 40X: 290.91 x 290.91 μm) at sequential excitation to prevent fluorophore bleed-
302 trough.

303

304

305 Image analysis

306 *In situ hybridisation signal:* Images of DAB- and haematoxylin-stained olfactory bulb sections were
307 obtained using a wide-field microscope with a 10X objective in RGB, so that the hematoxylin signal could
308 be separated into the blue channel. The same acquisition settings were used for all sections (*Tbx21*, *Lbhd2*
309 *and Pkib* signals). Dorsal, ventral, medial and lateral portions of the olfactory bulb at 3 anterior-posterior
310 locations were imaged so that all layers (nerve layer, glomerular layer, external plexiform layer, mitral cell
311 layer and GCL) were captured. To extract the positions of the external plexiform layer boundaries, in
312 ImageJ, a binary mask from the hematoxylin signal (blue) was obtained by setting a threshold and summed
313 along the axis parallel to the olfactory bulb layers. Hybridisation signal (DAB; red channel) was converted
314 into the binary mask, also by setting a single threshold across all conditions. Pixel co-ordinates were
315 normalised such that the boundaries of external plexiform layer were set from 0 – 1, with mitral cell layer
316 being 0. The density of the hybridisation signal was obtained by averaging the binary signal along the axis
317 parallel to the olfactory bulb layers.

318
319 *Soma detection and quantification for olfactory bulb:* Confocal images (1024 x 1024 pixels corresponding
320 to 425.1 μm x 425.1 μm) taken with a 20X objective were sampled at anterior, dorsal and ventral locations
321 of the mid-sagittal plane for the tdTomato signal using the *Ai14* reporter line, using the DAPI channel to
322 guide sampling, and 10 consecutive planes at a 100 μm interval for the virus injection experiment. Using
323 only the red and green channel for tdTomato labeling and EGFP labelling, respectively, somata were
324 detected manually in ImageJ using the ROI manager and their co-ordinates exported into Matlab, without
325 the observer knowing the identity of the mouse. External plexiform layer boundaries were demarcated
326 using only the DAPI signals from images, using a custom-written Matlab routine and the boundary co-
327 ordinates were stored. The soma depths from above were normalised along the external plexiform layer
328 using the boundary co-ordinates, such that the mitral cell layer was defined as 0, and the lower boundary
329 of the GL as 1. One-way ANOVA was used to compare the means, using the *anova1* function in Matlab,
330 and the *multcompare* function with the crucial value tested with Tukey's honest significant difference
331 criterion for *post-hoc* multiple comparisons. Cells belonging to mitral cell layer were defined as those
332 whose somata are positioned within 30% of the normalised external plexiform layer boundary from the
333 MC layer. This corresponded, on average, to 43.6 μm , which is equivalent to the lengths of two MC somata
334 (Nagayama et al., 2010). Thus, our measure takes into consideration the displaced MCs.

335
336 *Dendrite detection and quantification:* Images used were the same as those used to detect somata above.
337 To emphasise signals originating from dendrites, which are thin processes, background signal was
338 subtracted from the green or red channel using *Subtract Background* function in ImageJ, with the rolling
339 ball radius set to 5 pixels. Binary masks were created with a single threshold value and the presence of
340 the signal along the normalised external plexiform layer depth at each lateral position was averaged to
341 obtain the density. The dendritic preference index was used to compare the dendritic signal in the upper
342 external plexiform layer vs. lower external plexiform layer, as a proportion of the total dendritic signal
343 detected, calculated as $(\text{Signal_density}_{\text{upper_EPL}} - \text{Signal_density}_{\text{lower_EPL}}) / (\text{Signal_density}_{\text{upper_EPL}} +$
344 $\text{Signal_density}_{\text{lower_EPL}})$.

345
346 *Analysis of labelled MCs on a standardised coordinate:* Labelled MCs from coronal sections (1024 x 1024
347 pixels, 1.2 μm per pixel) were automatically detected in ImageJ by converting the red fluorescence image

348 into binary masks by thresholding and converted into ROIs using the Analyze Particles function (100 – 600
 349 pixels, circularity 0.1-1). The mitral cell layer was delineated using the DAPI channel in Matlab using the
 350 drawpolygon function. The line was interpolated, and labelled MCs were projected on the mitral cell layer
 351 coordinates. The centre of the olfactory bulb was calculated as the centre of the mitral cell layer
 352 coordinates. To pool data across mice, mitral cell layer coordinates were standardised such that it ran
 353 from $0 - 2\pi$ radians relative to the centre of the olfactory bulb.

354

355 *Whole brain somata detection:* Positions of somata labelled with tdTomato were automatically detected
 356 in the red channel of the stitched confocal images. To automatically detect the labelled somata,
 357 background fluorescence was subtracted using ImageJ's *Subtract Background* function (100 pixels), then
 358 further sharpened to accentuate the somata locally using ImageJ's *Unsharp* filter with the radius set to 14
 359 pixels, and mask weight set to 0.6. Then a binary mask was obtained by setting a threshold and the *Analyze*
 360 *Particles* function was used to detect round objects (size = 70-600 pixels, circularity 0.1 - 1), and detected
 361 structures added to the ROI manager, and exported as a list. Using the DAPI signals in the blue channel,
 362 boundaries of each nucleus was manually drawn in Matlab using the *drawpolygon* function. Finally, for
 363 each anatomical region, all detected soma positions within the boundary were counted using the *inROI*
 364 function and normalised by the area to standardise the density of detected cells per mm^2 . Distributions
 365 of labelled somata across strains were tested with 2-way ANOVA using Matlab's *anovan* function.

366

367 **Experimental Design and Statistical Analysis**

368 The Mann-Whitney U-test, t-test, Kolmogorov-Smirnov test, and 1-way- and 2-way-ANOVA were carried
 369 out using Matlab. Unless otherwise stated, t-tests were performed unpaired. Paired tests are described
 370 as "two-sample t-test" in the text. For *post-hoc* comparisons following significant ANOVA tests, the p-
 371 values are given in the following table for brevity of figure legends. Only the significant comparisons are
 372 listed due to the large number of pair-wise comparisons.

373

374 Table 1. *Details of post-hoc pair-wise statistical comparisons*

Figure	Test used	p-values
Figure 1H	1-way ANOVA followed by tukey-kramer multiple comparisons	P = 0.045 and 0.0086 for cluster 1 vs. cluster 2 and Cluster 2 vs. cluster 3, respectively for the null hypothesis that the two means do not differ.
Figure 2G	1-way ANOVA followed by tukey-kramer multiple comparisons	P = 0.0008 for <i>Tbx21</i> vs. <i>Lbhd2</i> ; 0.0035 for <i>Tbx21</i> vs. <i>Pkib</i> , respectively, for the null hypothesis that the two means do not differ.

Figure 7E, left panel	1-way ANOVA followed by tukey-kramer multiple comparisons	P = 0.012 for <i>Tbx21</i> vs. <i>Lbhd2</i> (1x80 mg/kg tamoxifen); 0.045 for <i>Tbx21</i> vs. <i>Lbhd2</i> (3x80 mg/kg tamoxifen); 0.008 for <i>Ra13</i> vs. <i>Lbhd2</i> (1x80 mg/kg tamoxifen); 0.029 for <i>Ra13</i> vs. <i>Lbhd2</i> (3x80 mg/kg tamoxifen), each for the null hypothesis that the two means do not differ.
Figure 7E, middle panel	1-way ANOVA followed by tukey-kramer multiple comparisons	P = 8.8×10^{-5} for <i>Tbx21</i> vs. <i>Lbhd2</i> (1x80 mg/kg tamoxifen); 1.5×10^{-5} for <i>Tbx21</i> vs. <i>Lbhd2</i> (3x80 mg/kg tamoxifen); 6.5×10^{-5} for <i>Ra13</i> vs. <i>Lbhd2</i> (1x80 mg/kg tamoxifen); 1.2×10^{-5} for <i>Ra13</i> vs. <i>Lbhd2</i> (3x80 mg/kg tamoxifen), each for the null hypothesis that the two means do not differ.
Figure 7E, right panel	1-way ANOVA followed by tukey-kramer multiple comparisons	P = 3.4×10^{-5} for <i>Tbx21</i> vs. <i>Lbhd2</i> (1x80 mg/kg tamoxifen); 1.1×10^{-4} for <i>Tbx21</i> vs. <i>Lbhd2</i> (3x80 mg/kg tamoxifen); 2.3×10^{-4} for <i>Ra13</i> vs. <i>Lbhd2</i> (1x80 mg/kg tamoxifen); 8.0×10^{-4} for <i>Ra13</i> vs. <i>Lbhd2</i> (3x80 mg/kg tamoxifen), each for the null hypothesis that the two means do not differ.

375

376

377

378

Data will be available upon request. *Lbhd2*-CreERT2 has been donated to the Jackson Laboratory Repository (stock number 036054).

379 **Results**

380

381 In search of molecular markers, we sought to compare the gene expression patterns of MCs and TCs. This may
382 reveal candidate markers, which are genes that are selectively enriched in the target cell-type of interest, in
383 this case MCs, but not expressed in other cell types. This first requires a method to identify MCs and TCs in a
384 gene expression data, and, second, distinguish their gene expression profiles from each other. Previous studies
385 observed that *Tbx21*, a T-box type transcription factor, labels both MCs and TCs (Faedo et al., 2002; Mitsui et
386 al., 2011; Haddad et al., 2013), while the neurotransmitter cholecystokinin (*Cck*) is more abundant in TCs
387 (Seroogy et al., 1985; Economo et al., 2016). To verify these distributions in our hands, we crossed *Tbx21-Cre*
388 and *Cck-IRES-Cre* lines (Taniguchi et al., 2011; Haddad et al., 2013) with the Rosa-CAG-LSL-tdTomato reporter
389 line, *Ai14* (Madisen et al., 2012), for Cre-dependent expression of the red fluorescent protein, tdTomato. We
390 confirm that *Tbx21*-driven expression labels cells in the mitral cell layer and the external plexiform layer where
391 TCs are located, while *Cck*-driven expression labels a larger number of cells all over the olfactory bulb (Fig. 1A-
392 C), especially those that extend more superficially in the glomerular layer and sporadically in the granule cell
393 layer. Importantly, labeling coupled to *Cck* expression is less consistent in cells that occupy the mitral cell layer.
394 These differential expression patterns between *Tbx21* and *Cck* may be used to distinguish MCs from TCs in
395 gene expression data (Fig. 1B,C).

396

397 Identification of molecular markers by differential expression analyses requires a robust and large dataset,
398 especially when distinguishing similar cell types, such as in the case of MCs and TCs. We turned to a public,
399 large scale scRNA-seq dataset of the mouse brain (Zeisel et al., 2018). This contains data from approximately
400 0.5 million cells, 10,745 cells of which are from the olfactory bulb. We clustered the data based on the
401 similarity of gene expression patterns. To achieve this efficiently, we identified the top 500 overdispersed
402 genes out of 27,998 genes in the dataset (see Methods; Fig. 1D). Such genes are highly informative for
403 determining genetic differences among the cells. Using this reduced dataset, we performed Principal
404 Component Analysis (PCA), followed by t-distributed Stochastic Neighbor Embedding (tSNE) on the first 10
405 principal components to further reduce the dimensionality of the gene expression space to two. The
406 combination of the two algorithms preserves both the global and local structures of the data (Kobak and
407 Berens, 2019). To obtain clusters, hierarchical density-based special clustering algorithm (HDBSCAN (Campello
408 et al., 2013)) was applied on the 2-dimensional tSNE space to cluster the data (see Methods). Within the
409 olfactory bulb dataset, we found that 1,682 cells belong to *Cck*-positive clusters, while *Tbx21*-expressing
410 cluster comprised 101 cells. Generally, expression patterns of *Cck* and *Tbx21* together mirror those of *Slc17a7*
411 (*VGlut1*) and *Slc17a6* (*Vglut2*), indicating that they are mainly glutamatergic populations (Fig. 1E,F), with the
412 largest portion of glutamatergic, *Cck*-positive clusters residing outside of the *Tbx21*-positive cluster. Further,
413 a small set of *Cck*-expressing neurons did not overlap with the *Slc17a7*-positive cluster (Fig. 1E,F). To identify
414 a putative mitral cell cluster from the scRNA-seq data, we took advantage of the observation that MCs and
415 TCs both express *Tbx21*, but *Cck* is more abundant among TCs. In the *Tbx21*-positive cluster, the second largest
416 cluster (cluster 2, Fig. 1G) showed the lowest *Cck* expression level (Fig. 1H). We thus refer to this as the putative
417 MC cluster, and refer to the remaining as TC cluster 1 (TC1).

418

419 An ideal molecular marker should be expressed abundantly and consistently in the cell type of interest, while
420 having minimal expression levels in other cell types. To search for candidates with these properties, gene

421 expression patterns of putative MCs were compared against the rest of *Tbx21*-expressing neurons (TC1; Fig.
422 2A), as well as glutamatergic, *Cck*-positive clusters outside of the *Tbx21*-cluster (TC2; Fig. 2A). First, the Mann-
423 Whitney U-test was used to screen genes that are differentially expressed, with p-values adjusted using the
424 Benjamini-Hochberg procedure. This procedure identified several differentially expressed genes (Table 2), at
425 the adjusted $p = 0.05$ level. Among these were *Calb2* (calbindin 2), *Ntng1* (netrin G1), *Ppm1j* (protein
426 phosphatase 1J), *Rph3a* (rabphilin 3A), *Kcnq3* (voltage-gated potassium channel subfamily Q member 3), and
427 *Chrna2* (cholinergic receptor nicotinic alpha 2). Of the differentially expressed genes, we focused on those
428 that are present in the majority (>50%) of cells in the putative MC cluster, but in less than 10% of the cells
429 outside of this cluster (Fig. 2B-H; Table 2). Only a small number of the differentially expressed genes fulfilled
430 these criteria, and even fewer showed minimal expression levels outside of MCs, as judged by the OB-wide
431 expression patterns (Fig 3A), as well as by the *in situ* hybridization data in the Allen Brain Atlas (Lein et al.,
432 2007). Candidate genes that showed clear hybridization signals outside of the mitral cell layer were therefore
433 not pursued further (Fig. 3B).

434
435 Based on the initial screening, *Pkib* (protein kinase inhibitor beta) and *Lbhd2* (LBH domain containing 2; Fig.
436 2C,D) genes fit the criteria for an MC marker. To confirm that these genes indeed are selectively expressed in
437 MCs, we carried out *in-situ* hybridization for *Pkib* and *Lbhd2* (Fig. 2B-D) on olfactory bulb sections. Indeed,
438 probes for *Pkib* and *Lbhd2* gave rise to monolayer-like signals at the lower boundary of the external plexiform
439 layer, corresponding to the location of the mitral cell layer. For quantification, *Pkib* and *Lbhd2* signals were
440 expressed as density (Methods) and plotted relative to the boundaries of the external plexiform layer. This
441 revealed that *Pkib* and *Lbhd2* both label cells in the MC layer, with significant reduction in the superficial signals
442 corresponding to TCs, especially compared to *Tbx21* (Fig. 2D; mean signal densities in the upper external
443 plexiform layer: *Tbx21* = 0.39 ± 0.007 ; *Lbhd2* = 0.005 ± 0.0002 ; *Pkib* = 0.01 ± 0.001 , $p = 0.0007$, 1-way ANOVA, $F =$
444 17.9 , degrees of freedom = 2). Hybridisation signal in the MCL was relatively uniform throughout the olfactory
445 bulb (Fig. 2H), while residual expression patterns of *Pkib* and *Lbhd2* in non-MC cells differed somewhat, with
446 faint signals in the glomerular layer and external plexiform layer for *Pkib* and *Lbhd2*, respectively. Thus, *Pkib*
447 and *Lbhd2* are promising candidates for selectively labelling MCs. On the other hand, the same analysis failed
448 to reveal clear molecular markers for sub-classes of TCs (Fig. 4).

449
450 Having identified candidate markers for MCs, we sought to test if Cre-recombinase expression from these loci
451 would allow MC-specific labeling. Screening several public depositories, we found a Cre-driver line for *Lbhd2*
452 under a synonymous gene symbol (A230065H16Rik) on GENSAT, a large repository of BAC-mediated
453 transgenic mouse lines (Heintz, 2004; Gong et al., 2007). Since the two independent Cre-driver lines (*Ra31-*
454 *Cre* vs. *Ra13-Cre*) show similar recombination patterns, we chose to analyse the line *Ra13-Cre*. As above, we
455 crossed *Ra13-Cre* mice with *Ai14* reporter mice to analyse the pattern of Cre-mediated recombination in the
456 brain (Fig. 5). At postnatal day 7 (P7), red fluorescence was highly selective, showing dense and restricted
457 expression in the cells of the MC layer of the olfactory bulb (Fig. 5A-C; mean number of fluorescent TCs as a
458 proportion of fluorescent cells in the mitral cell layer = 0.09 ± 0.04 for P7; $p = 0.18$, t-test for mean = 0, t-
459 statistic = 2; $n = 3$ mice). Correspondingly, labelled dendrites were observed preferentially in the lower portion
460 of the external plexiform layer (fluorescence signal density = 0.20 ± 0.03 for lower external plexiform layer vs.
461 0.10 ± 0.01 for upper external plexiform layer; $p = 0.03$, two-sample t-test for equal means, $n = 3$ mice each),
462 consistent with MCs having dendrites that ramify in the deeper portion of the external plexiform layer. At this

463 developmental stage, red fluorescence was observed only sparsely in the rest of the brain, except for the
464 lateral septum and the dorsomedial nucleus of the hypothalamus. However, in older mice, the residual
465 recombination becomes widespread and is observed throughout the brain. In the olfactory bulb at this stage,
466 while the labeling is still restricted to the projection neurons, a substantial number of tufted cells also become
467 labelled (mean number of fluorescent cells in the upper external plexiform layer as a proportion of fluorescent
468 cells in the mitral cell layer = 1.05 ± 0.08 for P21 and 1.33 ± 0.12 for P42). A Cre-driver line that we generated
469 for the second marker candidate, *Pkib*, was deemed unsuitable for MC-specific labeling due to late-onset
470 expression in MCs, as well as a wide-spread recombination in neurons other than MCs (Fig. 6).

471

472 The developmental accumulation described above makes *Ra13-Cre* unsuitable for investigating MCs in adult
473 mice. However, the *in-situ* hybridization signal for *Lbhd2* mRNA indicates a clear preference for MCs in the
474 adulthood. Therefore, it is possible that, when the recombination efficiency is calibrated appropriately, a more
475 selective labelling of MCs may be feasible. To this end, we generated a new knock-in line (Fig. 7A) using
476 CRISPR/Cas9, where the inducible Cre-recombinase, *Cre-ERT2* (Feil et al., 1997), is inserted into the 3'UTR of
477 the *Lbhd2* gene (the target sequence: 5'-ACCAAGAGGACCTCCAT-3'; Fig. 7A).

478

479 To test if selective labelling is maintained beyond P7 in the new, inducible Cre-driver line, we injected
480 tamoxifen intraperitoneally at P21 in *Lbhd2-CreERT2::Ai14* mice, and analysed the distribution of red
481 fluorescence 3 weeks post injection to assess the recombination pattern (Fig. 7B-E, Fig. 8A). At the lowest dose
482 tested (one injection of 80 mg/kg), the labeling was sparse (average density of labelled MCs = 5.7 ± 0.9 cells
483 per mm), but $83.7 \pm 3.7\%$ of labelled somata were located in the mitral cell layer (Fig. 7C,D). Other labelled
484 cells were mostly TCs, save for sporadic labeling in granule cells, which constituted about 1% of the labelled
485 cells. When the dose was increased to three intraperitoneal injections of tamoxifen (at 80 mg/kg *per diem*,
486 over three days), denser labeling was achieved (mean density = 10 ± 4 cells per mm; $78.0 \pm 11.0\%$ of labelled
487 somata were in MCL) while maintaining specificity, indicating that the tamoxifen dose can be calibrated to
488 titrate the specificity and density of labeling. Compared to the patterns of recombination observed with
489 existing lines, namely *Tbx21-Cre* and *Ra13-Cre* mice, overall, the new line achieves a labeling that is
490 substantially more selective for MCs, as measured by the positions of somata ($p = 0.016$, $F = 6.01$, 1-way
491 ANOVA; $n = 3$ mice for *Tbx21-Cre* and *Ra13-Cre*, 4 mice for *Lbhd2-IRES-CreERT2*) and dendrites ($p = 2.99 \times 10^{-6}$,
492 $F = 59.31$, 1-way ANOVA; $n = 3$ mice for *Tbx21-Cre* and *Ra13-Cre*, 4 mice for *Lbhd2-IRES-CreERT2*). Consistent
493 with the recombination pattern observed with the *Ra13-Cre* line, tamoxifen injection at P7 also resulted in a
494 mitral cell-specific labeling (Fig. 8B). To test if AAV-mediated conditional labeling is possible, AAV1-pCAG-Flex-
495 EGFP-WPRE (100 nL) was stereotaxically injected into the dorsal olfactory bulb at a depth of 300 μm below
496 the brain surface in P21 *Lbhd2-CreERT2::Ai14* mice. Tamoxifen injections (3 x 80mg/kg, i.p.) overlapped such
497 that the first of the three injections occurred immediately after the AAV injection. Three weeks later, labeling
498 pattern was analysed, which showed predominantly MC-selective labelling similar to the pattern obtained
499 with the *Ai14* reporter line (Fig. 8C).

500

501 Having achieved MC-selective labeling with the *Lbhd2-CreERT2* line, we wished to further characterize the
502 properties of the labelled cells in the olfactory bulb, as well as the distribution of labelled fibres in the olfactory
503 cortices (Fig. 9). Specifically, we wished to assess if the labelled MCs are present uniformly in all domains of

504 the olfactory bulb. To this end, confocal images from coronal sections from anterior, middle and caudal levels
505 of the olfactory bulb from *Lbhd2-CreERT2::Ai14* mice were analysed. This revealed consistent mitral cell layer
506 labeling in all regions of the olfactory bulb, except for the most anterior level, which tended to show a sparser
507 labeling on the medial side (Fig. 9B-D), though this was not statistically significant ($p = 0.56$, two-way ANOVA;
508 $n = 3$ mice). In terms of the projection patterns of labelled fibres in the olfactory cortices, we detected red
509 fluorescent fibres as fascicles throughout the antero-caudal extent of the lateral olfactory tract (Fig. 9A,B), as
510 well as thin fibers with bouton-like structures in the molecular layers of olfactory cortices, including in the
511 anterior olfactory nucleus, olfactory tubercle, and the anterior and posterior piriform cortices (Figure 9E-G).

512

513 In addition to the anatomical traits, to assess the labelled cells functionally, we loaded a synthetic calcium
514 indicator, Cal-520 dextran by electroporation (Fig. 10A) using a low intensity protocol (Hovis et al., 2010). Using
515 two-photon microscopy in mice anaesthetized with ketamine and xylazine, odour response properties of
516 labelled MCs vs. superficially located TCs were compared (Fig. 10A,B). As above, we used 42 day-old *Lbhd2-*
517 *CreERT2::Ai14* mice, where recombination was induced with tamoxifen (3×80 mg/kg) at P21. Consistent with
518 previous reports (Nagayama et al., 2010; Burton and Urban, 2014; Ackels et al., 2020; Eiting and Wachowiak,
519 2020), odours excited TCs more than labeled or unlabeled MCs (Fig. 10C,D). No obvious difference was
520 observed between labeled and unlabeled MCs. However, the lack of convincing responses raises some
521 questions about the identity of labelled cells. Localised loading of dyes by electroporation allows a direct
522 comparison of TCs and MCs belonging to the same glomerulus, but the low-yield and the low sensitivity of the
523 indicator are disadvantageous, especially when responses are sparse. To address this, we expressed GCaMP6f
524 conditionally by crossing the *Lbhd2-CreERT2* line with the *Ai95D* line (Madisen et al., 2015), with tamoxifen
525 injection at P21. Two weeks later, the injected mice were implanted with a cranial window over the left
526 olfactory bulb, and after two further weeks, the olfactory bulb was imaged with a two-photon microscope
527 under ketamine/xylazine anaesthesia. On average, 5-6 fluorescent cells were visible in a given field of view
528 ($256 \times 256 \mu\text{m}$) at a depth $\sim 300 \mu\text{m}$ below the brain surface (Fig. 10E). This time, a fraction of cell-odour pairs
529 (22.2%; $n = 270$ cell-odour pairs, 45 cells; 4 mice) exhibited robust fluorescence increases locked to odour
530 presentations (Fig. 10F), even though the majority of cells did not show detectable responses to any of the 6
531 odours presented (Fig. 10G). Overall, the results here indicate that the new inducible Cre-driver line, *Lbhd2-*
532 *CreERT2*, achieves a highly specific labeling of functional MCs in the olfactory bulb.

533

534 Finally, we examined the recombination pattern in the brain at large, beyond the olfactory bulb. To assess this,
535 we analysed the distribution of labelled somata in the anterior olfactory nucleus, olfactory tubercle, anterior
536 and posterior piriform cortex, and tenia tecta, as well as other, commonly studied regions, including the
537 thalamus, cerebellum, hippocampus and cerebral cortex. In the *Lbhd2-CreERT2* mice, for both doses of
538 tamoxifen tested, consistent labeling was observed unexpectedly in a small number of nuclei, including the
539 ventromedial nucleus of the hypothalamus and the lateral septum (Fig. 11- 12). Compared to the *Ra13-Cre*
540 driver line, the olfactory cortices were devoid of fluorescent cells (Figure 7C; no labelled cells were detected
541 for aPCx, pPCx, AON and OT in *Lbhd2-CreERT2::Ai14* mice; in *Ra13::Ai14* mice, mean density of labelled cells
542 = 91.2, 38.5, 490.2, 818.0 labelled cells per mm^2 for aPCx, pPCx, AON and OT, respectively; $p = 1.03 \times 10^{-38}$, $F =$
543 295.04, 2-way ANOVA, with mean densities for *Lbhd2-CreERT2* groups were significantly different from *Ra13-*
544 *Cre*; $n = 3$ mice per group). Thus, the results indicate that the labelling is, overall, relatively specific to MCs in

545 the whole brain, suggesting that the new inducible Cre-driver line may be suitable for a variety of studies to
546 investigate olfactory processing.

547 **Discussion**

548

549 A wide variety of neuron types that exist in the sensory systems are thought to reflect diverse components for
550 information processing in the brain (Masland, 2004; Luo et al., 2018). Availability of Cre-driver lines have led
551 to a multitude of fundamental insights into unique, cell-type specific contributions to sensory processing and
552 perception (Münch et al., 2009; Dhande et al., 2013; Cruz-Martín et al., 2014; Takahashi et al., 2020). Recent
553 progress in the acquisition, analyses, and applications of large-scale gene expression data have allowed
554 efficient analysis of the differences between cell-types of interest (Birnbaum, 2018; Luo et al., 2018). In this
555 study, we used a publicly available gene expression dataset to discover candidate molecular markers for the
556 key second-order cells of the olfactory system, MCs, which we validated with histology, and finally with new
557 Cre-driver lines generated by CRISPR/Cas9-mediated gene editing. We report that one driver line in particular
558 provides a substantial improvement in the ability to selectively label MCs.

559

560 Among the several candidates identified from our differential expression analysis, we found *Lbhd2* to be the
561 most promising. Specifically, at postnatal day 7, the recombination pattern for the non-inducible, *Ra13-
562 Cre::Ai14* is restricted mainly to MCs in the olfactory bulb. This pattern is consistent with the description on
563 the GENSAT expression database (Gong et al., 2007). Since TCs are already present and located superficially in
564 the external plexiform layer at this stage of development (Mizuguchi et al., 2012), this pattern likely reflects
565 genuine MC specificity in neonatal mice. Despite an increase in the sporadic *Lbhd2*-driven labelling of TCs and
566 other regions of the brain at later stages, the preferential expression in MCs over TCs that persists in adulthood
567 can be utilized to our advantage. Thus, with our new inducible Cre-driver line, the expression can be targeted
568 selectively to MCs even in the adulthood. It is notable that, despite the fact that many genes were differentially
569 expressed across the two cell types, markers suitable as genetic tools are harder to identify, especially when
570 selective expression is required across developmental stages. This difficulty may partly be due to the similarity
571 between MCs and TCs, and that cell types are often defined by a combination of genes, rather than single
572 genes (Luo et al., 2018).

573

574 In the olfactory bulb, labelled MCs were present in most domains of the olfactory bulb, except for a small
575 patch on the medial, anterior olfactory bulb that showed a curious lack of labeling. Whether or not these
576 correspond to subclasses of MCs, for example those that differ in the glomerular association (Li et al., 2017),
577 or cortical projection patterns (Zeppilli et al., 2020), will be intriguing for future investigation. Outside of the
578 olfactory bulb, labeled somata were sparse if not absent, especially in the areas that MCs target, including in
579 the anterior olfactory nucleus, olfactory tubercle, and the anterior and posterior piriform cortices. This makes
580 the *Lbhd2-CreERT2* line suitable for investigating the downstream, decoding mechanisms of mitral-specific
581 activity in all these areas, and also when imaging from boutons of MCs (Pashkovski et al., 2020). Beyond these
582 areas, however, we observed a small number of specific regions that showed the presence of labelled somata.
583 The areas include the lateral septum, ventromedial nucleus of the hypothalamus, and the medial amygdala,
584 even at the lowest dose of tamoxifen used. Thus, future studies using this line need to take this into account
585 when interpreting data, in particular for investigating innate, social behavior, which involve these areas
586 (Stowers and Liberles, 2016). However, the fact that only a subset of the nuclei in the pathways are labelled
587 may make this line unexpectedly useful for investigating mechanisms of social behaviour.

588

589 This study was aided by publicly accessible data, speeding up discovery. One limitation, if any, in using this
590 dataset for this study may have been the data size, where only a small fraction of olfactory bulb cells expressed
591 *Tbx21*, and even fewer belonged to the putative MC cluster. The relatively small MC cluster size may partly be
592 biological. Of the neurons present in the OB, approximately 80% are GABAergic. Further, glutamatergic
593 neurons comprise heterogeneous groups, including those that lack lateral dendrites (Hayar et al., 2004; Antal
594 et al., 2006). Thus, MCs comprise only a small proportion (~1%) of OB neurons (Burton, 2017; Schwarz et al.,
595 2018). Our histology indicates that superficially located, *Tbx21*-expressing cells are located below the
596 glomerular layer, unlike the *Cck*-expressing population that includes a dense population located more
597 superficially. It should also be noted that a large proportion of glutamatergic and *Cck*-expressing cells were
598 found outside of the *Tbx21*-positive cluster. Some of this latter group may correspond to external tufted cells,
599 which are glutamatergic but lack lateral dendrites (Macrides and Schneider, 1982). It is possible that protocols
600 used to obtain the scRNA-seq data may have been inadvertently biased against large cells with prominent
601 dendrites, such as the filtering step involving a pore size of 30 μm (Zeisel et al., 2018).

602

603 Despite the need for tamoxifen, this new method for labeling MCs has several advantages over the existing
604 methods. Currently, MC labeling and manipulations are achieved predominantly by depth, birthdate, or
605 retrograde viral expression utilizing the differential projection targets of MCs vs TCs (Haberly and Price, 1977;
606 Imamura et al., 2011; Rothermel et al., 2013; Economo et al., 2016). While this can indeed bias expression
607 patterns, the overlap in somatic and dendritic locations (Schwarz et al., 2018), as well as projection targets
608 (Haberly and Price, 1977; Igarashi et al., 2012) means that it is not trivial to achieve a highly selective labeling.
609 In contrast, our transgenic mouse line described here allows for reproducible and selective labeling of MCs
610 over TCs, with the added advantage that labelled MCs are located throughout the olfactory bulb. Even in
611 imaging applications that can distinguish the cell type based on the soma depth, with the new driver line, it
612 will be possible to investigate the physiology of subcellular compartments, such as the long lateral dendrites,
613 without the need to painstakingly trace back the structures to somata for cell-type identification. Similarly,
614 investigations of downstream decoding mechanisms, such as one involving precise optogenetic activations of
615 olfactory bulb projections using patterned light stimuli (Chong et al., 2020), may now be done in a cell-type
616 specific manner. Thus, our new tool may bring us closer to understanding how parallel olfactory processing
617 contributes to mechanisms of sensory perception and, ultimately, behaviour.

618

619

620

621

622

623

624

625

626

627 **Acknowledgement**

628 We would like to thank OIST's Imaging section, sequencing team, and AAALAC-accredited animal facility
629 staff for assistance, and Bernd Kuhn, Sander Lindeman and Gonzalo Otazu for comments on the
630 manuscript. This work was supported by the OIST Graduate University.

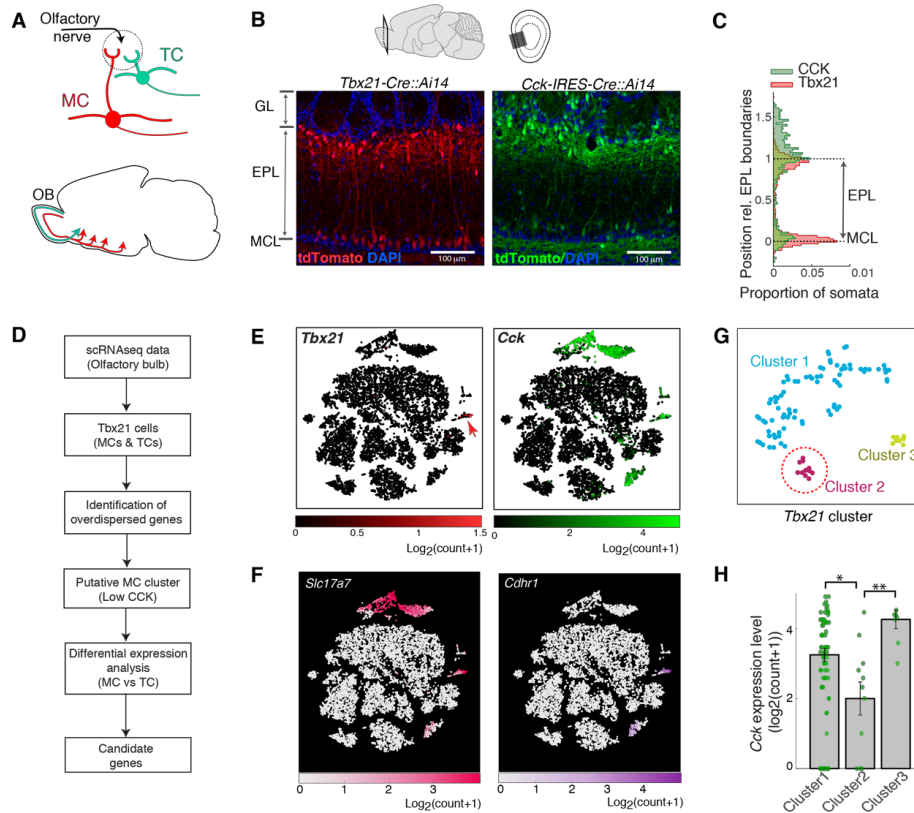
631

632 **Author contributions**

633 HM and IF conceived the project; AK, CZ, YPH and IF designed the experiments with help from HM and
634 JKR; CZ, YPH, TS, JKR & IF carried out the experiments; SM, FS and ST generated the transgenic mice; AK
635 and IF analysed the data with help from HM; and IF wrote the manuscript with inputs from all authors.

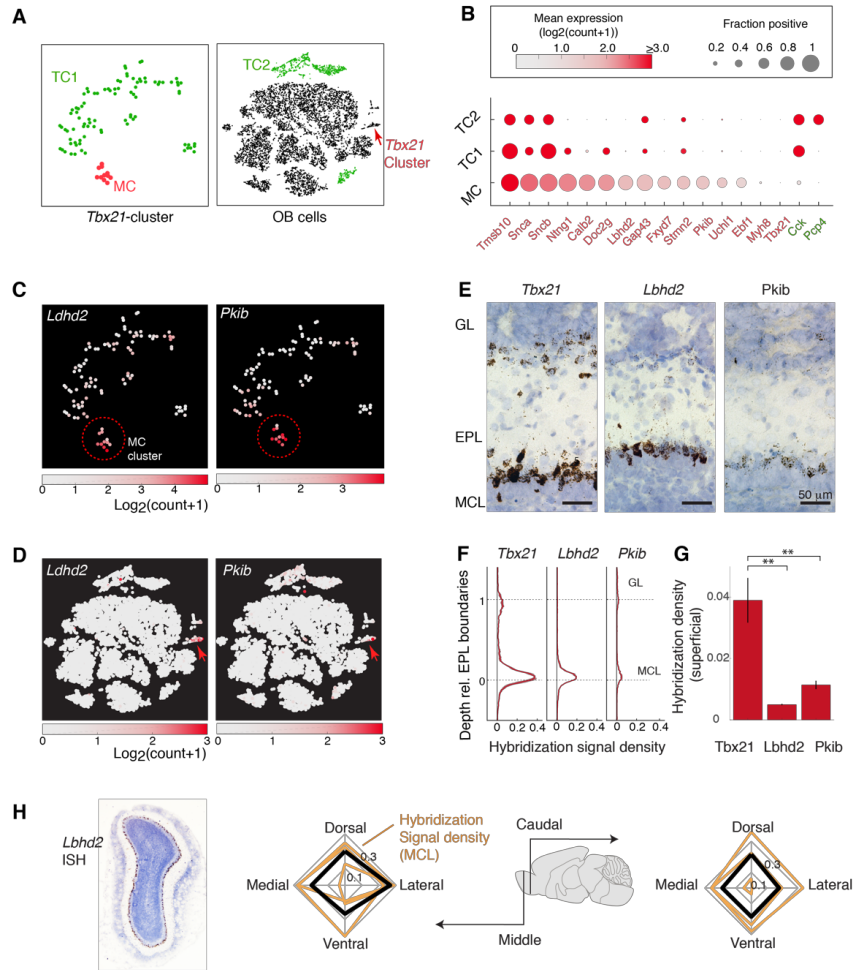
636

637 **Figures**



638
 639 **Figure 1: Strategy for identifying mitral-cell specific markers from scRNA-seq data**
 640 (A) Schematic showing major anatomical differences between the two cell types; MCs (red) are located deeper in
 641 the olfactory bulb (OB) layers, and project widely in olfactory cortices. TCs (green) are smaller, superficially located
 642 principal neurons that project to anterior portions of the olfactory cortex. (B) *Tbx21* and *Cck* expression patterns in
 643 the main olfactory bulb; example images showing tdTomato expression patterns in *Tbx21-Cre::Ai14* mouse (red)
 644 and *Cck-IRES-Cre::Ai14* mouse (green). Scale bar = 100 μ m. GL = glomerular layer, EPL = external plexiform layer,
 645 MCL = MC layer. (C) Soma positions of tdTomato-expressing cells relative to the EPL boundaries, for the images
 646 shown in B. EPL depth was normalized so that it ranged from 0 to 1, with the lower boundary (MCL) corresponding
 647 to 0. (D) Schematic of workflow; Putative mitral cluster from scRNA-seq data is identified by the observation that
 648 MCs and TCs both express *Tbx21*, but *Cck* is more abundant among TCs. Once putative MC and TC clusters were
 649 identified, differential expression analysis was carried out to identify genes that are selectively expressed in MCs.
 650 (E) OB cells plotted in tSNE coordinates, with *Tbx21* and *Cck* expression levels (left and right panels, respectively)
 651 indicated with colour maps shown below. (F) Expression levels of common markers for projection neurons of the
 652 OB; VGlut1 (*Slc17a7*) and *Cdhr1*. (G) *Tbx21*-positive cluster was further analysed and the sub-clustered and
 653 displayed in new tSNE coordinates. (H) *Cck* expression levels for the sub-clusters in (E). Cluster 2 has the lowest
 654 level and is inferred to be the putative MC cluster (red dotted line in E). Stars indicate a statistical significance at
 655 the 0.05 level (*) and 0.01 level (**). For details, see the Experimental Design and Statistical Analysis section.
 656

657

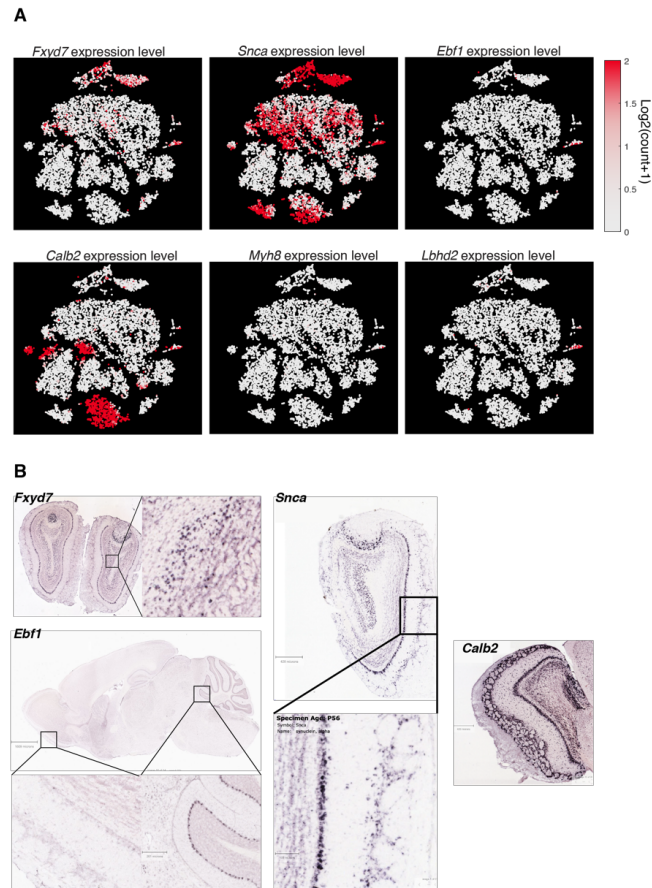


658
659
660
661
662
663
664
665
666
667
668
669
670
671

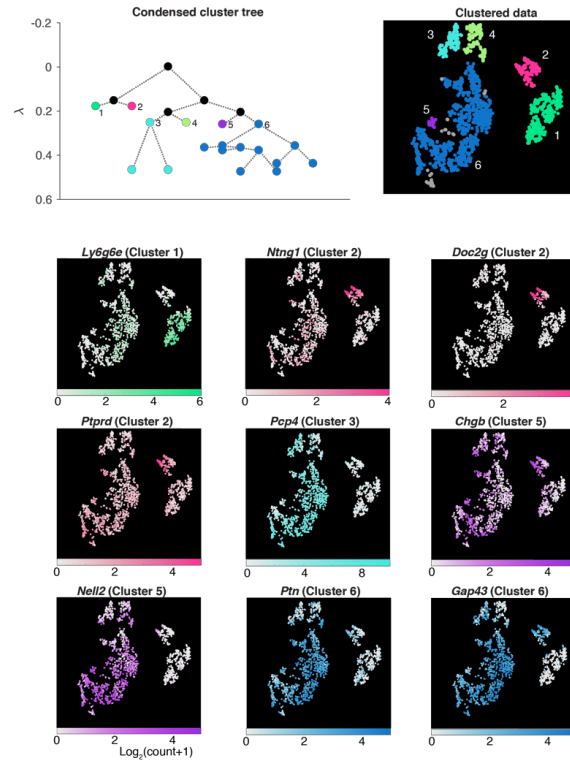
Figure 2: Differential gene expression analysis reveals candidate marker genes for MCs

(A) Cluster grouping used for differential gene expression analysis to distinguish TCs from MCs. *Tbx21* expressing cells (left) constitute the MC cluster (red) and TC1 cluster (green), which is identical to the combined clusters 1 and 3 shown in Fig. 1G. The olfactory bulb (OB)-wide dataset (right) contains the TC2 cluster (green) which is equivalent to the *Cck*-rich clusters shown in Fig. 1E without the *Tbx21*-rich clusters. (B) Genes that are significantly enriched in MCs (red), and TC clusters (green). The size of data points indicates the consistency of expression, measured as the fraction of cells in the cluster that express the gene. Mean expression level ($\log_2(\text{count}+1)$) is color-coded as shown in the colormap above. (C) Expression levels of two candidate genes, *Pkib* and *Lhd2*, with the corresponding colormaps, superimposed on the 3-sub clusters of the *Tbx21*-rich cluster (same tSNE coordinate as Figure 1G) and (D) the whole OB data. Red arrow points to the *Tbx21*-cluster. (E) Example *in-situ* hybridization signals revealed by DAB staining, for *Tbx21* (left), *Lhd2* (middle) and *Pkib* (right) for the MOB layers indicated. Scale bar = 50 μm . (F) *In-situ* hybridization signal density relative to the external plexiform layer boundary (0 – 1); hybridization signal was thresholded, and the proportion of pixels above the

672 threshold for each normalized external plexiform layer depth was expressed as density. **(G)** Summary of
673 hybridization signals in the superficial locations (depth upper half of external plexiform layer). N = 3 mice, with
674 samples from dorsal, ventral, medial and lateral locations at middle and caudal levels of the antero-caudal axis.
675 **(H)** Quantification of regional variation; average hybridization signal density from the MCL (right) for dorsal,
676 ventral, medial, and lateral samples taken from middle plane (bottom plot) and caudal plane (top plot) of the
677 antero-posterior axis. Orange lines correspond to data from individual mice, and black lines show the average
678 across the 3 mice.
679
680
681



682
 683 **Figure 3:** OB-wide tSNE data and *Allen Brain Atlas* ISH data used to screen candidate MC markers that were not
 684 analysed further.
 685 Differential expression analysis indicates that *Fxyd7*, *Ebf1*, *Snca*, *Calb2*, and *Myh8* are significantly enriched in MCs
 686 relative to TCs. (A) To screen candidates, the expression pattern (colormap) in the whole OB data were analysed.
 687 The same tSNE coordinates as in Fig. 1E,F are used, with *Lbhd2* expression pattern shown for comparison. (B)
 688 Further, the ISH database of the *Allen Brain Atlas* was used to assess the spatial expression patterns. *Fxyd7* seems
 689 to be expressed by neurons deep in the granule cell layer as well as superficial cells. *Snca* is expressed by some
 690 superficially located neurons as well as some neurons of the anterior olfactory nucleus. *Ebf1* is hardly detectable in
 691 the OB even though it is present in the Purkinje cell layer of the cerebellum. Dense *Calb2* hybridisation signal is
 692 visible in the glomerular layer, external plexiform layer, mitral cell layer, as well as the granule cell layer. *Myh8*
 693 signal was not described in the ISH database but it is a marker for somatostatin positive cells in the subventricular
 694 zone (Lim et al., 2018), which is the source of SST-positive interneurons of olfactory cortices. The expression data
 695 in (A) shows low levels of *Myh8* expression in many neurons outside of the *Vglut1*- and *2*-positive clusters. Image
 696 credit: Allen Institute.
 697
 698

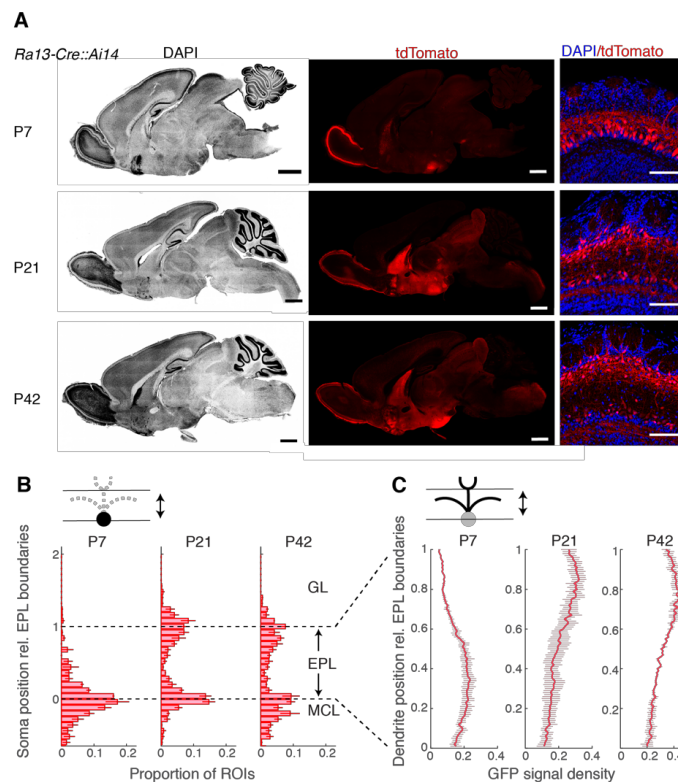


699
 700
 701
 702
 703
 704
 705
 706
 707
 708
 709

Figure 4: *Sub-clustering analysis of the Cck-expressing cluster*

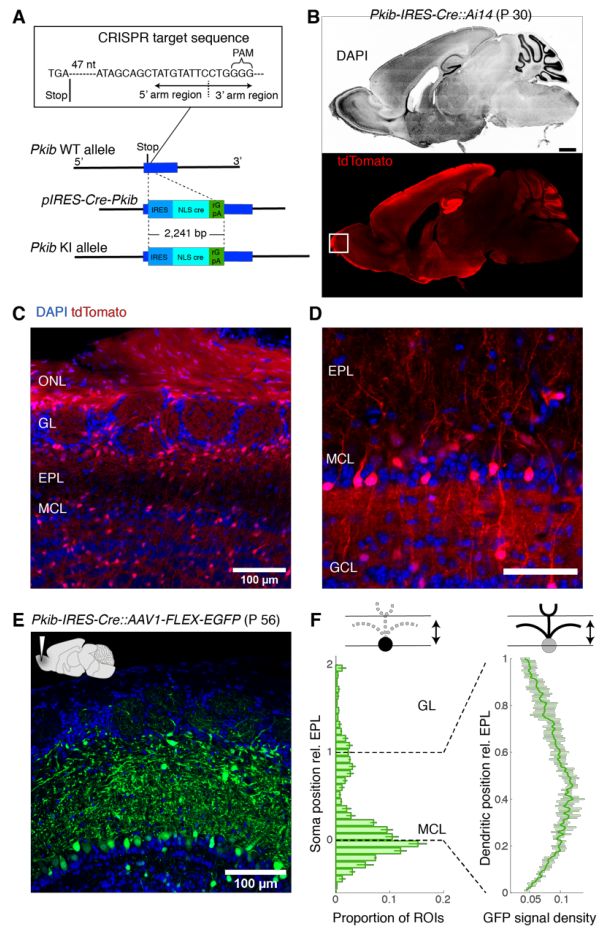
The Cck-expressing population from the OB dataset was further analysed to reveal sub-clusters. For each sub-cluster, candidate marker genes were identified by differential gene expression analysis, where expression patterns from a cluster of interest was compared against all other clusters combined. The expression patterns for each candidate marker, and in which sub-cluster the gene is enriched (in brackets), are shown for all cells in the Cck-positive population, with corresponding colormaps. While the Doc2g gene selectively labels the sub-cluster 2 in the TC-dataset, it is a gene that is also abundantly expressed by MCs (Fig. 2).

710



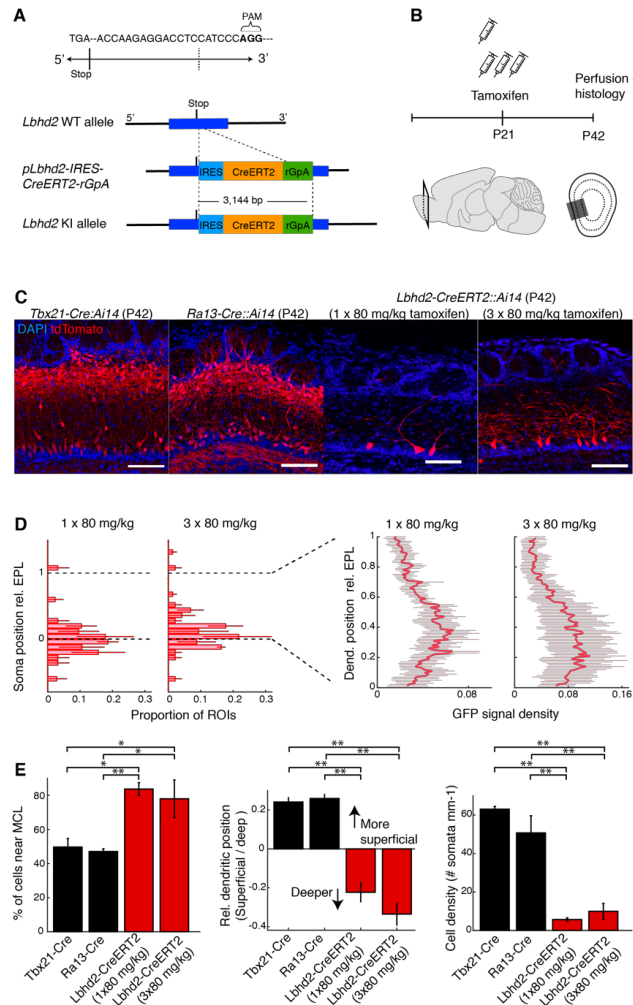
711
712
713
714
715
716
717
718
719

Figure 5: The *Ra13-Cre::Ai14* line reveals a developmental accumulation of recombination patterns outside of MCs (A) Sagittal brain sections from example P7 (top row), P21 (middle row) and P42 (bottom row) mice, showing DAPI signal (left column; pseudo-coloured in grey scale), corresponding tdTomato (middle column) and merged signals for OB (right column). Scale bar = 1 mm for the whole sagittal view, and 100 μ m for OB. (B) Distribution of somata positions with respect to the external plexiform layer boundaries. N = 3 mice (average of measurements from anterior, ventral and dorsal parts for each animal). (C) Distribution of labelled dendrites with respect to the external plexiform layer boundaries.



720
 721 **Figure 6:** *Pkib-IRES-Cre* labels a wide variety of non-MC neurons, with late onset labeling in MCs
 722 (A) Strategy for CRISPR/Cas9 – mediated generation of the *Pkib-IRES-Cre* transgenic mouse. The CRISPR-target
 723 sequence (inset) was just after the stop codon of the *Pkib* gene. Construct included sequences for IRES, Cre-
 724 recombinase with a nuclear localization signal, and rGpA. (B) Cre-mediated recombination pattern in a 30-day old
 725 *Pkib-IRES-Cre::Ai14* mouse. Structures visible in this sagittal plane is revealed by DAPI (top panel), and the
 726 corresponding pattern of recombination revealed by tdTomato signal. Scale bar = 0.5 mm. (C) tdTomato expression
 727 pattern relative to the OB layers from the same animal. ONL = olfactory nerve layer; GL = glomerular layer; EPL =
 728 external plexiform layer; MCL = mitral cell layer. Note the dense labeling of the ONL. (D) A higher magnification of
 729 image in C. Signals in the MCL are faint or lacking at this developmental stage. Scale bar = 0.1 mm. (E) A confocal
 730 image showing the EGFP expression pattern two weeks after an injection of AAV1-flex-EGFP into the MOB in a 42-
 731 day old *Pkib-IRES-Cre* mouse. (F) Summary of soma location (left) and dendritic signal density (right) relative to the
 732 EPL boundaries. Note the heavy presence of somata outside of the MCL and dendrites in the upper portion of the
 733 EPL.
 734
 735

736



737

738

739

740

741

742

743

744

745

746

747

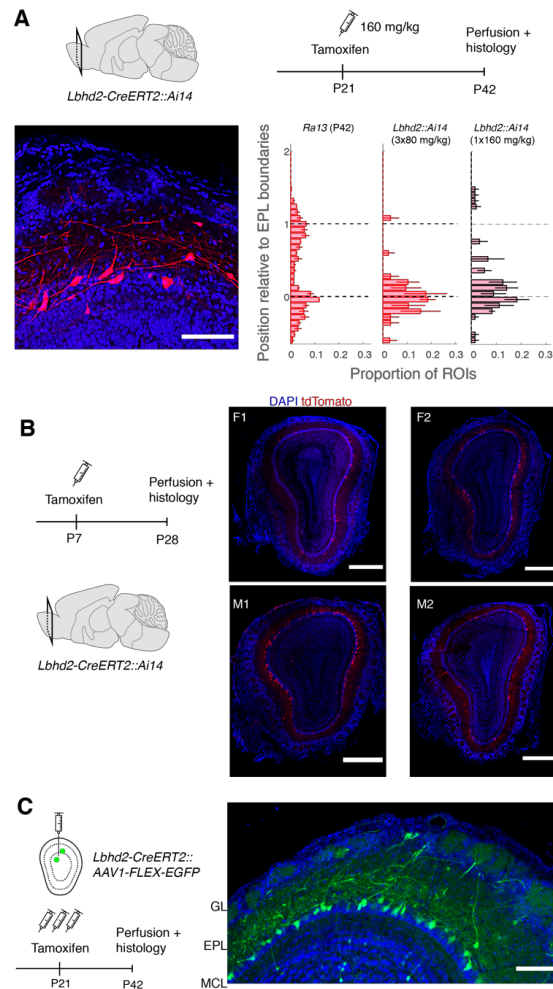
748

749

Figure 7: Lbhd2-CreERT2 line achieves MC-specific labeling in the olfactory bulb even in the adulthood

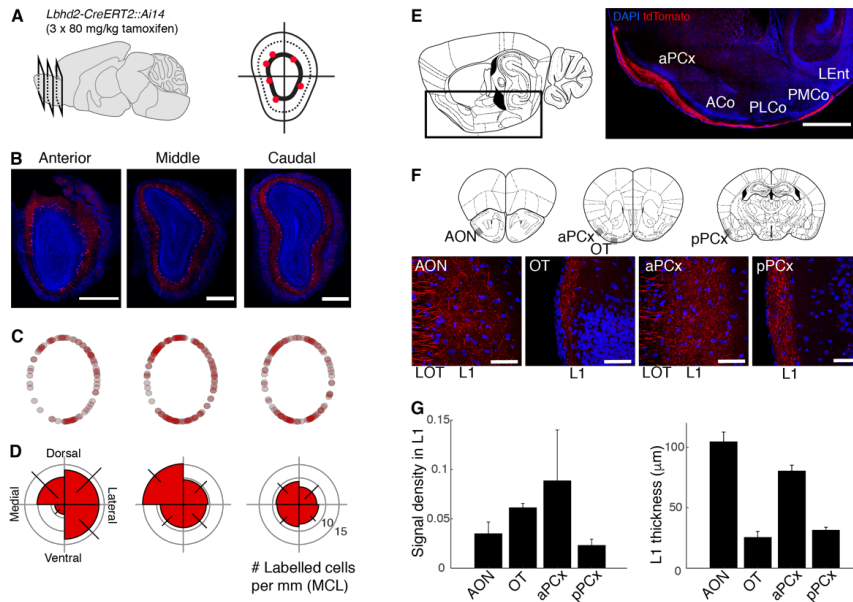
(A) Constructs for CRISPR/Cas9-mediated knock-in line. IRES-CreERT2 cassette was targeted to a region immediately following the stop codon of the Lbhd2 gene. (B) Schematic of the tamoxifen injection protocol: tamoxifen was injected intraperitoneally at P21, and the recombination pattern in the OB was examined 3 weeks later. Cohorts of mice received injection for either one or three days at 80 mg/kg per diem. (C) Example recombination patterns. From left: *Tbx21-Cre::Ai14*, *Ra13-Cre::Ai14*, *Lbhd2-CreERT2::Ai14* (one injection) and *Lbhd2-CreERT2::Ai14* (three injections). Scale bar = 100 μ m. (D) Summary of labelled structures at P42 for the corresponding mouse lines, showing the proportion of cells in the mitral cell layer relative to all labelled cells (left), comparison of labelled dendrites in the superficial vs. deep portions of the external plexiform layer (middle), and density of labelled somata in the mitral cell layer (right). (E) Comparison of labeling patterns between *Tbx21-Cre::Ai14*, *Ra13-Cre::Ai14* and *Lbhd2-CreERT2::Ai14* lines. Left: Labelled cells in the mitral cell layer as a percentage of total number of labelled cells. Middle: tdTomato signal density in the upper half of EPL subtracted by the signal density in the lower half of

750 EPL. Right: Number of labelled cells detected per mm of MCL. N = 3 mice per transgenic line for all plots. Mean and
751 s.e.m. shown. Stars indicate a statistical significance at the 0.05 level (*) and 0.01 level (**). For details, see the
752 Experimental Design and Statistical Analysis section.
753
754
755
756
757
758
759
760
761
762



763
 764 **Figure 8: Further characterization of tamoxifen-dependent recombination.**
 765 (A) Recombination pattern after 1 x 160 mg/kg at P21, with tdTomato analysed at P42. Scale bar = 0.1 mm. Bottom
 766 right: summary of labelled soma positions relative to the EPL layers in comparison to Ra13-Cre::Ai14 and Lbhd2-
 767 CreERT2::Ai14 (3 x 80 mg/kg). N = 3 mice. (B) Recombination pattern following tamoxifen-injection at P7. Lbhd2-
 768 CreERT2::Ai14 pups at post-natal day 7 were injected with a lowest dose tamoxifen (80 mg/kg intraperitoneally,
 769 once). Right: recombination patterns from 2 females (F) and 2 males (M), as indicated. Scale bar = 0.5 mm. (C)
 770 Tamoxifen-induced recombination with AAV-mediated expression. Tamoxifen (3 x 80 mg/kg) was administered
 771 intraperitoneally starting on the day of AAV (AAV1-flex-EGFP) injection in the dorsal OB and EGFP expression
 772 analysed three weeks later. Note that AAVs for conditional expression can exhibit Cre-independent, “leak
 773 expression” depending on the production protocol, (Fischer et al., 2019) or if not diluted enough.
 774

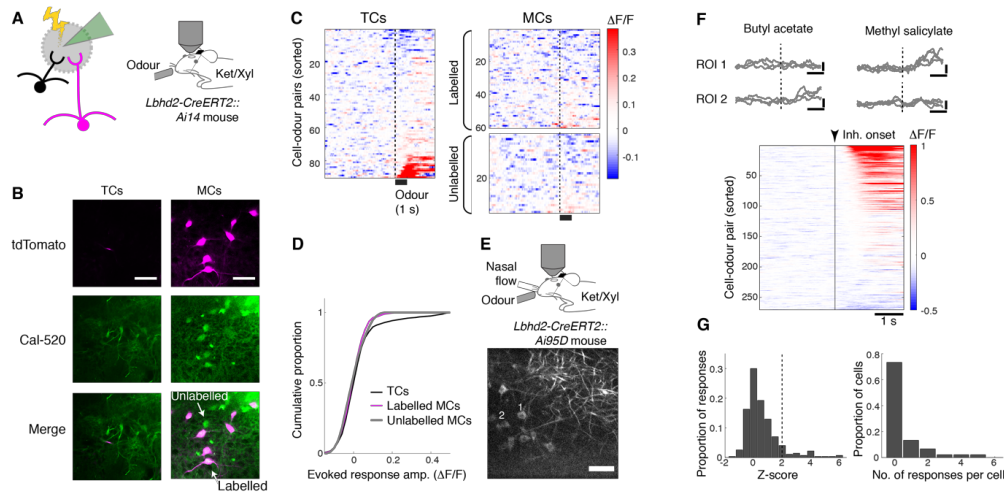
775



776
777
778
779
780
781
782
783
784
785
786
787
788
789
790
791
792
793
794
795

Figure 9: Properties of labelled MCs: OB domain-dependent variations and axon projection patterns
(A-D) Distribution of labelled MCs in the OB. **(A)** Schematic of analysis approach: positions of labelled MCs (red dots) were analysed for anterior, middle and caudal levels of the OB of Lbhd2-CreERT2::Ai14 mice (tamoxifen dose = 3 x 80 mg/kg). Angular positions were measured relative to the centre of the olfactory bulb. **(B)** Coronal OB images at each antero-posterior level from an example animal. Scale bar = 0.5 mm. **(C)** Positions of labelled MCs from all animals (one dot = one labelled MC), projected on a standardized mitral cell layer position (see Methods). N = 3 mice. **(D)** Polar histograms showing the number of labelled MCs per mm of mitral cell layer for each quadrant. Error bar = s.e.m. **(E-F)** Projection patterns of labelled fibres. **(E)** Image of a sagittal brain section (right) at the medio-lateral plane indicated in the illustration (left), with the imaged location marked by the black outline, showing tdTomato signal present in the lateral olfactory tract (LOT) and the molecular layer for the entire antero-caudal extent of the anterior piriform cortex (aPCx), anterior cortical amygdaloid nucleus (ACo), posterolateral cortical amygdaloid nucleus (PLCo), and posteromedial cortical amygdaloid nucleus (PMCo). Scale bar = 1 mm. **(F)** High magnification (40X objective) of coronal sections taken at the planes shown in illustrations (top). Grey boxes indicate approximate location of images below. Labelled fibres appear as fascicles in the LOT, while thinner, densely present labelled fibres are visible in the superficial, molecular layer (L1) for the anterior olfactory nucleus (AON), olfactory tubercle (OT), and the anterior and posterior piriform cortices (aPCx and pPCx, respectively). Scale bar = 50 μ m. **(G)** Summary quantification of signal density in the molecular layer for the 4 regions (left), and the thickness of the labelled L1 for the corresponding regions (right). N = 3 mice, one image plane each.

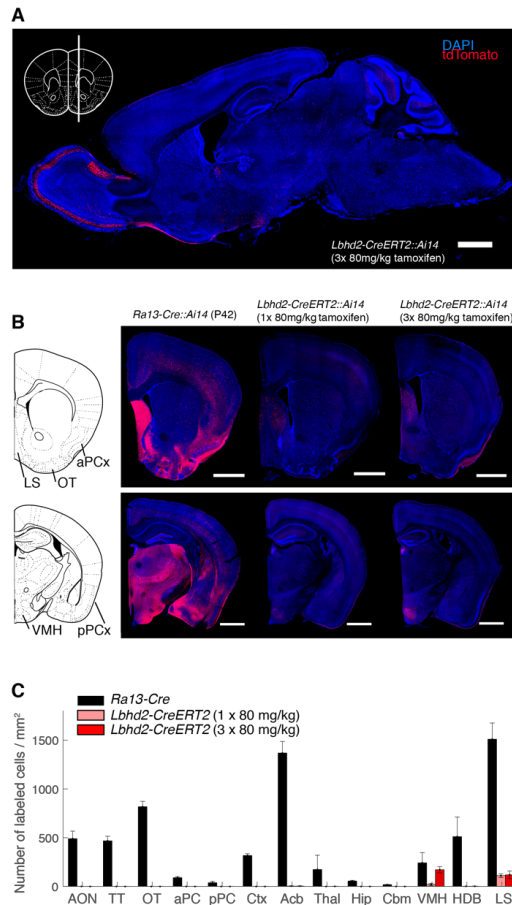
796



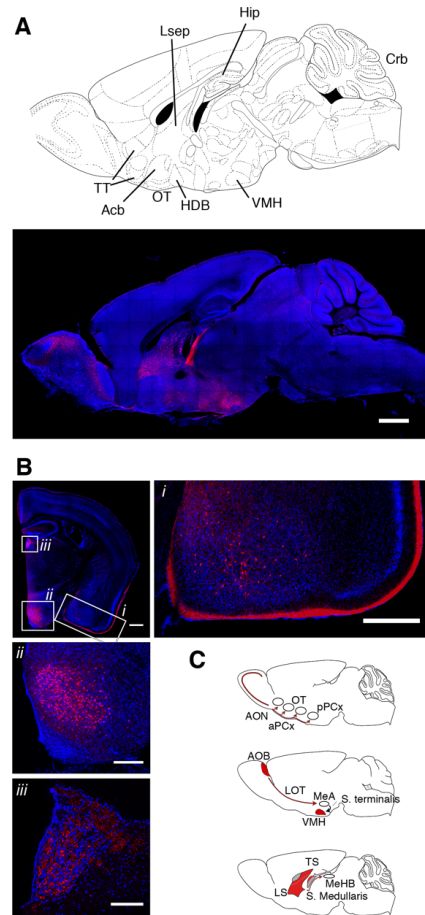
797
798
799
800
801
802
803
804
805
806
807
808
809
810
811
812
813
814
815
816
817

Figure 10: Odour response properties of labelled MCs, in comparison to TCs

(A) Schematic showing low intensity electroporation of Cal-520 dextran solution in the glomerular layer. (B) MCs were those located $\sim 300 \mu\text{m}$ below the brain surface, red fluorescence is pseudocoloured magenta (labeled = red fluorescent cells + green fluorescence, unlabeled = loaded cells without red fluorescence), while TCs were smaller cells located more superficially. Strongly fluorescent cells were excluded from analysis. Scale bar = $50 \mu\text{m}$. (C) Normalised fluorescence ($\Delta F/F$) from TCs (left) and labeled and unlabeled MCs (right, top and bottom, respectively), shown as colormap ($n = 2$ mice). Excitatory responses are more prevalent in TCs. Cal-520 has a lower affinity to Ca^{2+} than GCaMP6 variants, which may make hyperpolarizing responses to odours less detectable. (D) Cumulative histogram of response amplitude, for TCs (black), labeled MCs (magenta) and unlabeled MCs (grey). Overall distributions are not significantly different (two-sample K-S test; $p = 0.56$). (E) Top, experimental configuration; bottom, example field of view at a depth $\sim 280 \mu\text{m}$ below the brain surface. Scale bar = $50 \mu\text{m}$. (F) Top, example transients from two ROIs indicated in (E). Scale bars, vertical = $0.5 \Delta F/F$, horizontal = 1 s . Dotted line represents onset of the first inhalation after final valve opening. Bottom, summary of fluorescence change in response to odour presentations shown with a colormap ($n = 228$ cell-odour pairs, 38 cells, 3 mice). (G) Summary statistics of evoked responses; left, histogram of mean fluorescence change during odour (1 s from inhalation onset) expressed as Z-score for the data in (E); right, number of odours that each cell responds with a fluorescence increase (z-score greater than 2).



818
 819 **Figure 11: Brain-wide labeling is significantly reduced in the *Lbhd2-CreERT2* line.**
 820 (A) A sagittal view of an example brain from a P42 *Lbhd2-CreERT2* mouse, which received 3 doses of tamoxifen (80
 821 mg.kg⁻¹) at P21, showing DAPI (blue) and tdTomato (red) signals. Inset shows the medio-lateral plane for the sagittal
 822 section. Scale bar = 1 mm. (B) Example coronal images from *Ra13::Ai14* (left), and *Lbhd2-IRES-CreERT2::Ai14* mice
 823 that received 1 x tamoxifen and 3 x tamoxifen doses (middle and right, respectively). Illustrations on the left depict
 824 corresponding anatomical borders at this plane. Scale bar = 1 mm. (C) Summary showing average density of labeled
 825 cells for each anatomical region (n = 3 mice per region). Acb = Accumbens Nucleus (shell); AON = anterior olfactory
 826 nucleus; Cbm = cerebellum; Ctx = cerebral cortex; aPCx = anterior piriform cortex; HDB = nucleus of the horizontal
 827 limb of the diagonal band; Hip = hippocampus; LS = lateral septum; OT = olfactory tubercle; pPCx = posterior
 828 piriform cortex; Thal = thalamus; TT = tenia tecta; VMH = ventromedial nucleus of the hypothalamus.



829
 830 **Figure 12: Recombination pattern outside of the OB in *Lbhd2-CreERT2* mice**
 831 (A) A confocal image at a sagittal plane about 0.36 mm from the midline in a *Lbhd2-CreERT2::Ai14* mouse. Scale
 832 bar = 1 mm. (B) Coronal view at ~1.46 mm posterior to the Bregma, showing (i) labelled cells in the basolateral
 833 amygdaloid nucleus, fibre endings in the molecular layer medial amygdaloid nucleus and posterior piriform
 834 cortex; (ii) densely labelled somata in the ventromedial nucleus of the hypothalamus and (iii) labelled fibres in
 835 the medial habenular nucleus. (C) Summary of labelled structures with respect to distinct pathways; Top, MCs
 836 of the main olfactory bulb are labelled, but not their cortical targets. Middle; principal neurons of the accessory
 837 olfactory bulb are labelled. Labelled fibres, but not somata, are visible in the medial amygdaloid nucleus. The
 838 target of the medial amygdaloid nucleus, namely, the ventromedial nucleus of the hypothalamus, has densely
 839 labelled cells. Bottom, lateral septum densely contains labelled cells; the output fiber tracts are strongly
 840 labelled (stria medullaris), and labelled fibres are clearly visible in the target structure, namely, the medial
 841 habenular nucleus.

842 Table 2: List of genes differentially expressed between mitral cells and tufted cells.
 843

Gene Name	Mean Expression (log ₂ (count+1))	Adjusted p value
Myh8	2.14	1.57E-09
Pkib	3.40	7.02E-06
Fxyd7	3.66	1.41E-05
A230065H16Rik (Ldbh2)	3.77	1.55E-05
Ebf1	2.55	1.55E-05
Calb2	4.60	1.55E-05
Snca	5.10	1.55E-05
C1ql1	2.53	1.55E-05
Cxcl14	0.42	1.55E-05
Sostdc1	0.36	2.07E-05
Tmsb10	6.12	3.05E-05
Spp1	2.20	3.45E-05
Ntng1	4.76	4.25E-05
RP23-407N2.2	1.81	4.70E-05
1110008P14Rik	2.45	0.000163822
Tspan17	1.99	0.000211554
Uchl1	3.24	0.000253744
Shisa3	1.98	0.000253744
Gap43	3.69	0.000439148
Ppm1j	1.85	0.000449468
Rph3a	0.74	0.000449468
Crtac1	1.97	0.000449468
Tnnc1	0.27	0.000457871
Mmp17	0.45	0.000585813
Nov	0.18	0.000707168
Gng13	1.03	0.001406527
Rab15	1.62	0.001959665
Gm27199	1.11	0.001978521
Vsnl1	0.83	0.002521565
Stmn2	3.57	0.003524909
Npr1	1.30	0.003848843
Doc2g	4.52	0.004924184
Nptxr	0.78	0.005760704
Kcnq3	0.94	0.005928465
Slc1a2	1.29	0.007685702

Sncb	4.97	0.00781742
Ephx4	1.37	0.009259688
Atp9a	1.91	0.009383075
Nrsn1	2.65	0.01005383
Diras2	1.50	0.01094975
Rgs4	0.76	0.01098611
AI413582	2.09	0.0124281
Abi3bp	0.09	0.01393499
Lingo1	1.67	0.01393499
Tshz2	3.22	0.01393499
Mal2	0.18	0.01393499
Fkbp1b	0.00	0.01393499
Prkcb	1.23	0.01504482
Cdh4	1.02	0.01504482
Meg3	7.01	0.01660475
Chrna3	0.61	0.01660475
Ifitm10	0.74	0.01905793
Adk	0.34	0.02020242
Stx1a	0.89	0.02020242
Igfbp5	2.75	0.02381658
Fam19a1	0.09	0.0261028
Grin1os	0.09	0.0261028
Cdc20	0.09	0.0261028
Gm26803	0.09	0.0261028
Resp18	1.14	0.0261028
Pantr1	1.12	0.02678842
Lmo4	0.91	0.02690157
Pvrl1	1.07	0.03585761
Kitl	0.00	0.0397583

844

845

846

847

848 **References**

849

850 Ackels T, Jordan R, Schaefer AT, Fukunaga I (2020) Respiration-Locking of Olfactory Receptor and
851 Projection Neurons in the Mouse Olfactory Bulb and Its Modulation by Brain State. *Frontiers in*
852 *Cellular Neuroscience* 14.

853 Antal M, Eyre M, Finklea B, Nusser Z (2006) External tufted cells in the main olfactory bulb form two
854 distinct subpopulations. *Eur J Neurosci* 24:1124-1136.

855 Birnbaum KD (2018) Power in Numbers: Single-Cell RNA-Seq Strategies to Dissect Complex Tissues.
856 *Annual Review of Genetics* 52:203-221.

857 Bochkov YA, Palmenberg AC (2006) Translational efficiency of EMCV IRES in bicistronic vectors is
858 dependent upon IRES sequence and gene location. *Biotechniques* 41:283-292.

859 Burton SD (2017) Inhibitory circuits of the mammalian main olfactory bulb. *Journal of Neurophysiology*
860 118:2034-2051.

861 Burton SD, Urban NN (2014) Greater excitability and firing irregularity of tufted cells underlies distinct
862 afferent-evoked activity of olfactory bulb mitral and tufted cells. *The Journal of Physiology*
863 592:2097-2118.

864 Campello RJGB, Moulavi D, Sander J (2013) Density-Based Clustering Based on Hierarchical Density
865 Estimates. In: *Advances in Knowledge Discovery and Data Mining* (Pei J, Tseng VS, Cao L, Motoda
866 H, Xu G, eds), pp 160-172: Springer Berlin Heidelberg.

867 Chong E, Moroni M, Wilson C, Shoham S, Panzeri S, Rinberg D (2020) Manipulating synthetic optogenetic
868 odors reveals the coding logic of olfactory perception. *Science* 368:eaba2357.

869 Cong L, Ran FA, Cox D, Lin S, Barretto R, Habib N, Hsu PD, Wu X, Jiang W, Marraffini LA, Zhang F (2013)
870 Multiplex Genome Engineering Using CRISPR/Cas Systems. *Science* 339:819.

871 Cruz-Martín A, El-Danaf RN, Osakada F, Sriram B, Dhande OS, Nguyen PL, Callaway EM, Ghosh A,
872 Huberman AD (2014) A dedicated circuit links direction-selective retinal ganglion cells to the
873 primary visual cortex. *Nature* 507:358-361.

874 Daigle TL et al. (2018) A Suite of Transgenic Driver and Reporter Mouse Lines with Enhanced Brain-Cell-
875 Type Targeting and Functionality. *Cell* 174:465-480.e422.

876 Dhande OS, Estevez ME, Quattrochi LE, El-Danaf RN, Nguyen PL, Berson DM, Huberman AD (2013)
877 Genetic Dissection of Retinal Inputs to Brainstem Nuclei Controlling Image Stabilization. *The*
878 *Journal of Neuroscience* 33:17797.

879 Economo MN, Hansen KR, Wachowiak M (2016) Control of Mitral/Tufted Cell Output by Selective
880 Inhibition among Olfactory Bulb Glomeruli. *Neuron* 91:397-411.

- 881 Eiting TP, Wachowiak M (2020) Differential Impacts of Repeated Sampling on Odor Representations by
882 Genetically-Defined Mitral and Tufted Cell Subpopulations in the Mouse Olfactory Bulb. *The*
883 *Journal of Neuroscience* 40:6177.
- 884 Faedo A, Ficara F, Ghiani M, Aiuti A, Rubenstein JLR, Bulfone A (2002) Developmental expression of the
885 T-box transcription factor T-bet/Tbx21 during mouse embryogenesis. *Mechanisms of*
886 *Development* 116:157-160.
- 887 Feil R, Wagner J, Metzger D, Chambon P (1997) Regulation of Cre Recombinase Activity by Mutated
888 Estrogen Receptor Ligand-Binding Domains. *Biochemical and Biophysical Research*
889 *Communications* 237:752-757.
- 890 Fischer KB, Collins HK, Callaway EM (2019) Sources of off-target expression from recombinase-
891 dependent AAV vectors and mitigation with cross-over insensitive ATG-out vectors. *Proceedings*
892 *of the National Academy of Sciences* 116:27001.
- 893 Fukunaga I, Berning M, Kollo M, Schmaltz A, Schaefer Andreas T (2012) Two Distinct Channels of
894 Olfactory Bulb Output. *Neuron* 75:320-329.
- 895 Geramita MA, Burton SD, Urban NN (2016) Distinct lateral inhibitory circuits drive parallel processing of
896 sensory information in the mammalian olfactory bulb. *eLife* 5:e16039.
- 897 Gong S, Doughty M, Harbaugh CR, Cummins A, Hatten ME, Heintz N, Gerfen CR (2007) Targeting Cre
898 Recombinase to Specific Neuron Populations with Bacterial Artificial Chromosome Constructs.
899 *The Journal of Neuroscience* 27:9817.
- 900 Gong S, Zheng C, Doughty ML, Losos K, Didkovsky N, Schambra UB, Nowak NJ, Joyner A, Leblanc G,
901 Hatten ME, Heintz N (2003) A gene expression atlas of the central nervous system based on
902 bacterial artificial chromosomes. *Nature* 425:917-925.
- 903 Haberly LB, Price JL (1977) The axonal projection patterns of the mitral and tufted cells of the olfactory
904 bulb in the rat. *Brain Research* 129:152-157.
- 905 Haddad R, Lanjuin A, Madisen L, Zeng H, Murthy VN, Uchida N (2013) Olfactory cortical neurons read out
906 a relative time code in the olfactory bulb. *Nature Neuroscience* 16:949.
- 907 Hayar A, Karnup S, Ennis M, Shipley MT (2004) External Tufted Cells: A Major Excitatory Element That
908 Coordinates Glomerular Activity. *The Journal of Neuroscience* 24:6676.
- 909 Heintz N (2004) Gene Expression Nervous System Atlas (GENSAT). *Nature Neuroscience* 7:483-483.
- 910 Hovis KR, Padmanabhan K, Urban NN (2010) A simple method of in vitro electroporation allows
911 visualization, recording, and calcium imaging of local neuronal circuits. *Journal of Neuroscience*
912 *Methods* 191:1-10.
- 913 Igarashi KM, Ieki N, An M, Yamaguchi Y, Nagayama S, Kobayakawa K, Kobayakawa R, Tanifuji M, Sakano
914 H, Chen WR, Mori K (2012) Parallel Mitral and Tufted Cell Pathways Route Distinct Odor
915 Information to Different Targets in the Olfactory Cortex. *The Journal of Neuroscience* 32:7970.

- 916 Imamura F, Ayoub AE, Rakic P, Greer CA (2011) Timing of neurogenesis is a determinant of olfactory
917 circuitry. *Nature Neuroscience* 14:331-337.
- 918 Jordan R, Fukunaga I, Kollo M, Schaefer AT (2018) Active Sampling State Dynamically Enhances Olfactory
919 Bulb Odor Representation. *Neuron* 98:1214-1228.e1215.
- 920 Kapoor V, Provost AC, Agarwal P, Murthy VN (2016) Activation of raphe nuclei triggers rapid and distinct
921 effects on parallel olfactory bulb output channels. *Nature Neuroscience* 19:271.
- 922 Kobak D, Berens P (2019) The art of using t-SNE for single-cell transcriptomics. *Nature Communications*
923 10:5416.
- 924 Larsson LI, Rehfeld JF (1979) Localization and molecular heterogeneity of cholecystokinin in the central
925 and peripheral nervous system. *Brain Research* 165:201-218.
- 926 Lein E, Borm LE, Linnarsson S (2017) The promise of spatial transcriptomics for neuroscience in the era
927 of molecular cell typing. *Science* 358:64.
- 928 Lein ES et al. (2006) Genome-wide atlas of gene expression in the adult mouse brain. *Nature* 445:168.
- 929 Lein ES et al. (2007) Genome-wide atlas of gene expression in the adult mouse brain. *Nature* 445:168-
930 176.
- 931 Li H, Horns F, Wu B, Xie Q, Li J, Li T, Luginbuhl DJ, Quake SR, Luo L (2017) Classifying *Drosophila* Olfactory
932 Projection Neuron Subtypes by Single-Cell RNA Sequencing. *Cell* 171:1206-1220.e1222.
- 933 Lim L, Pakan JMP, Selten MM, Marques-Smith A, Llorca A, Bae SE, Rochefort NL, Marín O (2018)
934 Optimization of interneuron function by direct coupling of cell migration and axonal targeting.
935 *Nature Neuroscience* 21:920-931.
- 936 Luo L, Callaway EM, Svoboda K (2018) Genetic Dissection of Neural Circuits: A Decade of Progress.
937 *Neuron* 98:256-281.
- 938 Macrides F, Schneider SP (1982) Laminar organization of mitral and tufted cells in the main olfactory
939 bulb of the adult hamster. *Journal of Comparative Neurology* 208:419-430.
- 940 Madisen L, Zwingman TA, Sunkin SM, Oh SW, Zariwala HA, Gu H, Ng LL, Palmiter RD, Hawrylycz MJ,
941 Jones AR, Lein ES, Zeng H (2010) A robust and high-throughput Cre reporting and
942 characterization system for the whole mouse brain. *Nature Neuroscience* 13:133-140.
- 943 Madisen L et al. (2012) A toolbox of Cre-dependent optogenetic transgenic mice for light-induced
944 activation and silencing. *Nature Neuroscience* 15:793.
- 945 Madisen L et al. (2015) Transgenic Mice for Intersectional Targeting of Neural Sensors and Effectors with
946 High Specificity and Performance. *Neuron* 85:942-958.
- 947 Masland RH (2004) Neuronal cell types. *Current Biology* 14:R497-R500.

- 948 Mitsui S, Igarashi KM, Mori K, Yoshihara Y (2011) Genetic visualization of the secondary olfactory
949 pathway in Tbx21 transgenic mice. *Neural Systems & Circuits* 1:5.
- 950 Mizuguchi R, Naritsuka H, Mori K, Yoshihara Y (2012) Tbr2 Deficiency in Mitral and Tufted Cells Disrupts
951 Excitatory–Inhibitory Balance of Neural Circuitry in the Mouse Olfactory Bulb. *The Journal of*
952 *Neuroscience* 32:8831.
- 953 Mizuno S, Dinh TTH, Kato K, Mizuno-Iijima S, Tanimoto Y, Daitoku Y, Hoshino Y, Ikawa M, Takahashi S,
954 Sugiyama F, Yagami K-i (2014) Simple generation of albino C57BL/6J mice with G291T mutation
955 in the tyrosinase gene by the CRISPR/Cas9 system. *Mammalian Genome* 25:327-334.
- 956 Mori K, Kishi K, Ojima H (1983) Distribution of dendrites of mitral, displaced mitral, tufted, and granule
957 cells in the rabbit olfactory bulb. *Journal of Comparative Neurology* 219:339-355.
- 958 Münch TA, da Silveira RA, Siegert S, Viney TJ, Awatramani GB, Roska B (2009) Approach sensitivity in the
959 retina processed by a multifunctional neural circuit. *Nature Neuroscience* 12:1308-1316.
- 960 Nagai Y, Sano H, Yokoi M (2005) Transgenic expression of Cre recombinase in mitral/tufted cells of the
961 olfactory bulb. *genesis* 43:12-16.
- 962 Nagayama S, Enerva A, Fletcher M, Masurkar A, Igarashi K, Mori K, Chen W (2010) Differential Axonal
963 Projection of Mitral and Tufted Cells in the Mouse Main Olfactory System. *Frontiers in Neural*
964 *Circuits* 4:120.
- 965 Otazu Gonzalo H, Chae H, Davis Martin B, Albeanu Dinu F (2015) Cortical Feedback Decorrelates
966 Olfactory Bulb Output in Awake Mice. *Neuron* 86:1461-1477.
- 967 Papaioannou VE, Silver LM (1998) The T-box gene family. *BioEssays* 20:9-19.
- 968 Pashkovski SL, Iurilli G, Brann D, Chicharro D, Drummey K, Franks KM, Panzeri S, Datta SR (2020)
969 Structure and flexibility in cortical representations of odour space. *Nature* 583:253-258.
- 970 Pfeiffer CK, Xue M, He M, Huang ZJ, Scanziani M (2013) Inhibition of inhibition in visual cortex: the logic
971 of connections between molecularly distinct interneurons. *Nature Neuroscience* 16:1068.
- 972 Phillips ME, Sachdev RNS, Willhite DC, Shepherd GM (2012) Respiration Drives Network Activity and
973 Modulates Synaptic and Circuit Processing of Lateral Inhibition in the Olfactory Bulb. *The Journal*
974 *of Neuroscience* 32:85.
- 975 Rothermel M, Brunert D, Zabawa C, Díaz-Quesada M, Wachowiak M (2013) Transgene Expression in
976 Target-Defined Neuron Populations Mediated by Retrograde Infection with Adeno-Associated
977 Viral Vectors. *The Journal of Neuroscience* 33:15195.
- 978 Sanes JR, Masland RH (2015) The Types of Retinal Ganglion Cells: Current Status and Implications for
979 Neuronal Classification. *Annual Review of Neuroscience* 38:221-246.
- 980 Schwarz D, Kollo M, Bosch C, Feinauer C, Whiteley I, Margrie TW, Cutforth T, Schaefer AT (2018)
981 Architecture of a mammalian glomerular domain revealed by novel volume electroporation
982 using nanoengineered microelectrodes. *Nature Communications* 9:183.

- 983 Seroogy KB, Brecha N, Gall C (1985) Distribution of cholecystokinin-like immunoreactivity in the rat main
984 olfactory bulb. *Journal of Comparative Neurology* 239:373-383.
- 985 Shekhar K, Lapan SW, Whitney IE, Tran NM, Macosko EZ, Kowalczyk M, Adiconis X, Levin JZ, Nemes J,
986 Goldman M, McCarroll SA, Cepko CL, Regev A, Sanes JR (2016) Comprehensive Classification of
987 Retinal Bipolar Neurons by Single-Cell Transcriptomics. *Cell* 166:1308-1323.e1330.
- 988 Short SM, Wachowiak M (2019) Temporal Dynamics of Inhalation-Linked Activity across Defined
989 Subpopulations of Mouse Olfactory Bulb Neurons Imaged *In Vivo*. *eneuro* 6:ENEURO.0189-
990 0119.2019.
- 991 Ståhl PL et al. (2016) Visualization and analysis of gene expression in tissue sections by spatial
992 transcriptomics. *Science* 353:78.
- 993 Stowers L, Liberles SD (2016) State-dependent responses to sex pheromones in mouse. *Current Opinion*
994 *in Neurobiology* 38:74-79.
- 995 Sugino K, Hempel CM, Miller MN, Hattox AM, Shapiro P, Wu C, Huang ZJ, Nelson SB (2006) Molecular
996 taxonomy of major neuronal classes in the adult mouse forebrain. *Nature Neuroscience* 9:99-
997 107.
- 998 Takahashi N, Ebner C, Sigl-Glöckner J, Moberg S, Nierwetberg S, Larkum ME (2020) Active dendritic
999 currents gate descending cortical outputs in perception. *Nature Neuroscience* 23:1277-1285.
- 1000 Tang F, Barbacioru C, Wang Y, Nordman E, Lee C, Xu N, Wang X, Bodeau J, Tuch BB, Siddiqui A, Lao K,
1001 Surani MA (2009) mRNA-Seq whole-transcriptome analysis of a single cell. *Nature Methods*
1002 6:377.
- 1003 Taniguchi H, He M, Wu P, Kim S, Paik R, Sugino K, Kvitsani D, Fu Y, Lu J, Lin Y, Miyoshi G, Shima Y, Fishell
1004 G, Nelson Sacha B, Huang ZJ (2011) A Resource of Cre Driver Lines for Genetic Targeting of
1005 GABAergic Neurons in Cerebral Cortex. *Neuron* 71:995-1013.
- 1006 Tasic B et al. (2016) Adult mouse cortical cell taxonomy revealed by single cell transcriptomics. *Nature*
1007 *Neuroscience* 19:335.
- 1008 van der Maaten L, Hinton G (2008) Visualizing Data using t-SNE. *Journal of Machine Learning Research*
1009 9:2579-2605.
- 1010 Wang F, Flanagan J, Su N, Wang L-C, Bui S, Nielson A, Wu X, Vo H-T, Ma X-J, Luo Y (2012) RNAscope: a
1011 novel in situ RNA analysis platform for formalin-fixed, paraffin-embedded tissues. *J Mol Diagn*
1012 14:22-29.
- 1013 Wolff SBE, Gründemann J, Tovote P, Krabbe S, Jacobson GA, Müller C, Herry C, Ehrlich I, Friedrich RW,
1014 Letzkus JJ, Lüthi A (2014) Amygdala interneuron subtypes control fear learning through
1015 disinhibition. *Nature* 509:453.
- 1016 Zeisel A, Muñoz-Manchado AB, Codeluppi S, Lönnerberg P, La Manno G, Juréus A, Marques S, Munguba
1017 H, He L, Betsholtz C, Rolny C, Castelo-Branco G, Hjerling-Leffler J, Linnarsson S (2015) Cell types
1018 in the mouse cortex and hippocampus revealed by single-cell RNA-seq. *Science* 347:1138.

- 1019 Zeisel A, Hochgerner H, Lönnerberg P, Johnsson A, Memic F, van der Zwan J, Häring M, Braun E, Borm LE,
1020 La Manno G, Codeluppi S, Furlan A, Lee K, Skene N, Harris KD, Hjerling-Leffler J, Arenas E, Erfors
1021 P, Marklund U, Linnarsson S (2018) Molecular Architecture of the Mouse Nervous System. *Cell*
1022 174:999-1014.e1022.
- 1023 Zeng H, Sanes JR (2017) Neuronal cell-type classification: challenges, opportunities and the path
1024 forward. *Nature Reviews Neuroscience* 18:530.
- 1025 Zeppilli S, Ackels T, Attey R, Klimpert N, Boeing S, Crombach A, Schaefer A, Fleischmann A (2020)
1026 Molecular characterization of projection neuron subtypes in the mouse olfactory bulb.
1027 bioRxiv:2020.2011.2030.405571.
1028